

Femtosecond and Attosecond Light Sources and Techniques for Spectroscopy

Lukas Gallmann and Ursula Keller

Physics Department, ETH Zürich, Zürich, Switzerland

1 INTRODUCTION

The drive to resolve faster and faster dynamics in physical or chemical systems has been one of the main motivations for the development of sources of ultrashort optical pulses. While improved microscopic tools allow us to study matter down to the level of a single atom, the advent of ultrashort laser pulse technology enabled time-resolved studies of processes such as molecular vibration or chemical reaction dynamics (see Frey *et al.* 2011: **High-resolution Rotational Raman Coherence Spectroscopy with Femtosecond Pulses**, this handbook). With state-of-the-art sources reaching ~ 100 as ($1 \text{ as} = 10^{-18} \text{ s}$) pulse duration in the extreme ultraviolet (XUV) spectral region, even the potentially extremely fast dynamics of such a lightweight particle as the electron has become accessible (see Wörner and Corkum 2011: **Attosecond Spectroscopy**, this handbook).

While the human eye is incapable of resolving any motion occurring on a timescale shorter than ~ 0.1 s, mechanical camera shutters allow us to extend our observations beyond the millisecond range. Direct electronic detection expands our observation range to below a nanosecond. However, only ultrashort laser pulses provide a general method to access the natural timescales of molecular, atomic, and even electronic processes.

The extremely short duration of ultrashort optical pulses brings along that they concentrate moderate amounts of energy into a very brief time window. As a result, peak powers can reach above a megawatt in pulses directly produced by a laser oscillator. With the additional amplification

of the pulses, peak powers can raise into the terawatt and even petawatt range. Owing to the excellent focusability of laser light, not only high peak powers but also high intensities can be obtained. High intensities translate into high field strengths of the electromagnetic fields forming the laser beam. Beyond time-resolving ultrafast dynamics, these unique properties of ultrashort laser pulses enable a wide variety of applications.

Many of these properties are also exploited for spectroscopic applications. The high intensities can induce a nonlinear response in an optical medium. In most time-resolved spectroscopy arrangements, such a nonlinear response is used to temporally gate and thereby resolve the signal of interest.

Ultrashort optical pulses are also being used to actively control molecular systems (Rabitz *et al.* 2000). Adaptively optimizing the evolution of the system into a desired direction (e.g., selecting one of several possible dissociation pathways) by varying the shape of the ultrashort pulses provides another method to study the properties of the system. In such coherent-control experiments, one extracts information about the studied process by analyzing the pulse shapes needed to obtain a certain outcome of this process.

Complementary to the time-domain structure of ultrashort laser pulses, one finds that the extremely regular pulse train produced by a laser oscillator corresponds to an evenly spaced grid of narrow, equidistant frequencies in the spectral domain. These so-called frequency combs enable new precision levels in high-resolution frequency metrology and spectroscopy (Eikema and Ubachs 2011: **Precision Laser Spectroscopy in the Extreme Ultraviolet**, this handbook).

In this article, we review femtosecond and attosecond light sources and their underlying technology. Owing to

their wide variety, we limit the discussion to the most commonly used femtosecond pulse sources. We briefly describe only the techniques that are used to apply the pulse sources in spectroscopy. As it is the case for femtosecond sources, spectroscopic techniques are available in many different flavors (*see* Frey *et al.* 2011: **High-resolution Rotational Raman Coherence Spectroscopy with Femtosecond Pulses** and Wörner and Corkum 2011: **Attosecond Spectroscopy**, this handbook). We thus concentrate on the basic concepts underlying most of these methods. This article is intended as a starting point and reference to help the reader gain the required knowledge for a more in-depth study of a special topic of interest found elsewhere in this handbook or in the literature.

The article is divided into three main parts: femtosecond laser technology, femtosecond techniques, and high-order harmonic generation (HHG). In the section dealing with femtosecond laser technology, we describe various sources of femtosecond laser pulses, their properties, and the technology behind these sources. First, we introduce the most important optical pulse forming processes that play a relevant role in the femtosecond domain. The understanding of these basic processes is the key to the technology presented in the remainder of this section. We start the discussion of the actual femtosecond laser technology with pulsed oscillators that forms part of every time-resolved spectroscopy setup. If the pulse energy obtained from the oscillator is not sufficient, amplifier systems are used to boost the energy into the desired range. A short overview of ultrashort pulse amplifiers is given. We then introduce the concepts of the carrier-envelope offset phase (CEP) and frequency combs. Frequency combs are a quite recent addition to the spectroscopic tool set provided by femtosecond laser technology. Because classical laser materials do not cover all the wavelength ranges of interest for spectroscopic studies, we give an overview of parametric sources. In particular for the extension toward the visible and the infrared spectral regions, nonlinear frequency conversion based on parametric processes is often the only option.

We then discuss femtosecond measurement techniques. We focus on the general concepts that are shared by most time-resolved spectroscopy methods. Examples that illustrate how these concepts are transferred to practical experiments are found elsewhere in this handbook (*see* Frey *et al.* 2011: **High-resolution Rotational Raman Coherence Spectroscopy with Femtosecond Pulses** and Wörner and Corkum 2011: **Attosecond Spectroscopy**, this handbook). Ultrashort pulse characterization can be considered as a special case of time-resolved measurements: measurements with the goal of determining the shape of the ultrashort optical pulse itself. While ultrashort pulse characterization is an essential tool in every ultrafast science laboratory, its description also provides insight into how

time-resolved methods work and how such measurement schemes can be implemented. We limit the discussion to the most commonly used characterization techniques.

A strong focus of current research is the extension of time-resolved spectroscopy into the attosecond time domain (*see* Wörner and Corkum 2011: **Attosecond Spectroscopy**, this handbook). We devote the last part of this article to describe the technology and the current state-of-the-art of attosecond sources. The fundamental process leading to the generation of attosecond pulses is HHG. This is a highly nonlinear process in which coherent light with a high (odd) integer multiple of the driving laser's photon energy is produced. The resulting light is typically located in the vacuum ultraviolet (VUV) to soft-X-ray spectral region. As a consequence of the spectral location of the attosecond pulses, the time-resolved measurement techniques typically need to be implemented somewhat differently compared to the visible-to-infrared spectral region familiar from femtosecond technology. As it is the case in the femtosecond domain, attosecond pulse characterization can be understood as a subset of attosecond time-resolved tools. We discuss the present approaches that have been implemented successfully. Finally, we give an outlook toward the extension of time-resolved spectroscopic techniques to higher photon energies beyond the soft-X-ray spectral region.

Because a description of femtosecond and attosecond light sources and technology can never be exhaustive in the limited space available in this article, we hope to provide the reader with the most relevant technologies and a solid starting ground for further exploration. Throughout this article, references to extensive review papers are given that offer further details to the interested reader.

2 FEMTOSECOND LASER TECHNOLOGY

In the following, we review the fundamental technology behind the laser sources required to perform ultrafast spectroscopy. We concentrate on the most common technologies. However, most of the important concepts introduced in this paragraph are also present in more unusual pulse sources that may be found elsewhere in the literature. Our discussion is limited to sources in the femtosecond domain.

2.1 Basic Pulse Forming Processes

This paragraph covers the most essential physical processes that take place in femtosecond optical pulse sources: dispersion, self-phase modulation (SPM), gain, and loss. They are sufficient to explain pulse formation and shaping

in most pulse generation scenarios. A solid understanding of these effects is also a prerequisite for the proper design of any experimental setup involving ultrashort optical pulses. More detailed information on the physics of ultrashort optical pulse propagation can be found in the classical book by Agrawal (2001).

2.1.1 Dispersion

A plane electromagnetic wave traveling through a linear optical medium experiences a phase shift of $\varphi(z) = k_n \cdot z$ as a function of propagation coordinate z . In a homogenous optical medium with refractive index n , the wavenumber k_n is given by $k_n = n \cdot c/\omega$, where c denotes the speed of light in vacuum and ω represents the angular frequency of the plane wave (note that we neglect absorption in the medium such that n becomes a real valued quantity). An extension of these relations to inhomogeneous optical media is straightforward by incorporating a z -dependence in to the refractive index n . In a medium with absorption or optical gain, only the real part of n contributes to the phase shift, whereas the imaginary part modifies the wave amplitude.

If we now consider an ultrashort optical pulse as a linear superposition of plane waves with differing angular frequency ω , the various waves constituting the pulse will generally experience different phase shifts as they propagate through the medium. This can be a consequence of the angular velocity dependence of k_n or different geometrical path lengths traveled by the various wave components (e.g., due to angular dispersion in refraction or diffraction) or a combination thereof. The angular frequency dependent phase shift $\varphi(\omega)$ can be expanded into a Taylor series around the center angular frequency ω_0 of the pulse

$$\begin{aligned} \varphi(\omega) = & \varphi_0 + \left. \frac{\partial \varphi}{\partial \omega} \right|_{\omega_0} (\omega - \omega_0) + \frac{1}{2} \left. \frac{\partial^2 \varphi}{\partial \omega^2} \right|_{\omega_0} (\omega - \omega_0)^2 \\ & + \frac{1}{6} \left. \frac{\partial^3 \varphi}{\partial \omega^3} \right|_{\omega_0} (\omega - \omega_0)^3 + \dots \end{aligned} \quad (1)$$

$T_g := \partial\varphi/\partial\omega$ is usually referred to as *group delay* or *first-order dispersion*, $D := \partial^2\varphi/\partial\omega^2$ is the group delay dispersion (GDD) or second-order dispersion, and $\partial^3\varphi/\partial\omega^3$ denotes the third-order dispersion (TOD). When analyzing the effect of the different derivatives on the pulse, one finds that the constant term φ_0 describes an offset between the carrier wave of the pulse and its envelope. A change in the group delay corresponds to a time delay of the pulse without affecting its shape. Thus, only second and higher order terms have an impact on the temporal intensity profile of the pulse. Because the GDD is the first derivative of the group delay, it represents a linear variation of group delay with frequency. As a result, its effect is to separate

or concentrate frequency components in time, depending on the sign of the GDD and the initial relation between the different frequency components at the input to the medium. Figure 1 illustrates the effect of GDD and TOD. The left graph shows a pulse with all frequency components aligned at a fixed time (this is called a *transform-limited pulse*, equivalent to the quadratic and all higher order terms in equation (1) being zero). The effect of the positive GDD applied to the pulse is to advance all lower frequencies in time and delay all higher frequencies. The result is a positive “chirp” (or “up-chirp”) of the pulse. Negative GDD would create a negative “chirp” (“down-chirp”). The impact on the pulse shape is that it symmetrically broadens compared to the case without GDD. On the other hand, TOD asymmetrically distorts the pulse. With pure positive TOD, all frequencies deviating from the center frequency are delayed in time. Interference between the delayed pulse components leads to oscillations of the temporal intensity profile in the trailing part of the pulse. The same magnitude of negative TOD would result in a time-reversed version of the graph (it is generally correct that a flip of the sign of $\varphi(\omega)$ is equivalent to time reversal).

As a rule of thumb for pulses with a center wavelength around 800 nm (e.g., pulses from a Ti:sapphire laser) and for typical amounts of dispersion present in an experimental setup, one finds that GDD starts to play a significant role for transform-limited pulse durations below approximately 100 fs, while TOD becomes relevant below ~ 30 fs. For pulse durations below 10 fs, higher order dispersion terms also need to be considered. For an initially transform-limited (or “unchirped”) Gaussian pulse with full width at half maximum (FWHM) pulse duration τ_0 , one finds that the effect of GDD alone increases the pulse duration according to the following equation:

$$\tau = \tau_0 \cdot \sqrt{1 + \left(4 \ln 2 \frac{D}{\tau_0^2}\right)^2} \approx D \cdot \Delta\omega \quad (2)$$

The approximation on the right hand side of equation (2) holds in the limit of strong pulse broadening, with $\Delta\omega$ denoting the spectral FWHM of the pulse.

In the visible to near-infrared spectral region at wavelengths shorter than the zero-dispersion wavelength, i.e., the wavelength at which GDD vanishes, all transparent optical materials exhibit positive GDD. The zero-dispersion wavelength of quartz glass is located at $\sim 1.3 \mu\text{m}$ and that of most other typical optical materials are close to that value. As a result, it is not possible to compensate for dispersive pulse spreading by inserting some negative GDD material into the beam path. However, there are several methods that make use of the geometrical path length dependence

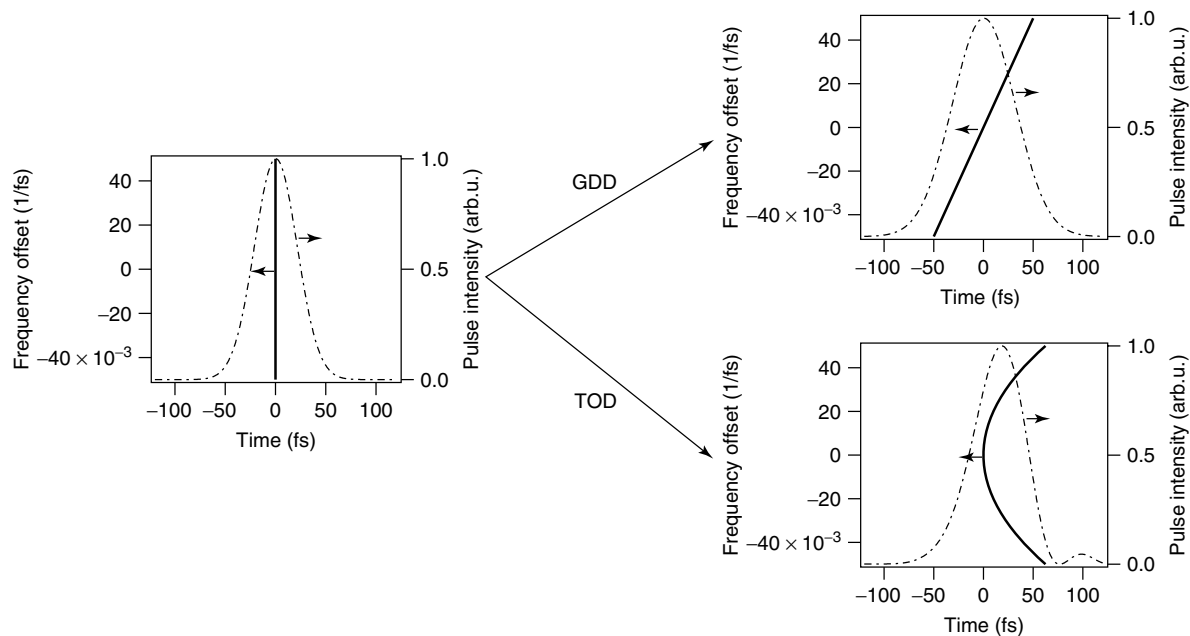


Figure 1 This figure illustrates the effect of GDD and TOD on an initially transform-limited pulse. The solid line visualizes the delay experienced by all frequency components with respect to the center frequency ω_0 of the pulse. The dash-dotted line shows the effect on an actual pulse intensity profile. The initial pulse has a Gaussian profile with 50-fs full width at half maximum pulse duration. 1000 fs^2 of GDD and $50\,000 \text{ fs}^3$ of TOD have been applied in each respective case. Where GDD results in a symmetric pulse broadening, TOD creates an asymmetric pulse profile with an oscillating trailing wing.

of $\varphi(\omega)$ or multibeam interference effects to achieve effective negative GDD between the input and the output plane of such a device.

The most common dispersion compensation schemes used in the femtosecond pulse duration regime are schematically depicted in Figure 2. Both the grating and the prism compressor make use of angular dispersion to create the desired path length differences for the various frequency components of the pulse. For the grating compressor, angular dispersion is a result of diffraction, whereas in the case of the prism compressor it is due to refraction. It can be shown that angular dispersion always results in a negative contribution to the GDD of a setup, independent of the spectral range or the dispersive properties of the components (Martinez *et al.* 1984).

The grating compressor introduced by Treacy (1969) is the method of choice if large amounts of GDD need to be introduced or compensated for. At the first grating, the beam is spectrally dispersed with the low frequencies (“red”) experiencing a larger diffraction angle than the high frequencies (“blue”). After diffraction off the second grating, the individual frequency components travel parallel to each other. The third and the fourth grating serve to obtain again a spatially coherent beam for which all spectral components are aligned collinearly on top of each other. A mirror can be placed between the second and the third grating (dashed line in Figure 2a) to fold the setup into

a two-grating design. Normally, the overall transmission efficiency of a broadband grating compressor is not very high, which prevents its use for intra-cavity dispersion compensation in an ultrafast laser oscillator. The bandwidth of the gratings and the large amounts of higher order dispersion introduced by a grating compressor limit its use to pulse durations above ~ 30 fs.

The prism compressor provides less GDD for a similar footprint than a typical grating compressor (Fork *et al.* 1984). The individual prisms are cut for a symmetric optical path and Brewster angle incidence at the center wavelength of the pulse. As a result of the Brewster condition, prism compressors introduce very little losses, and are therefore ideally suited for intra-laser-cavity dispersion compensation. As it was the case for the grating compressor, the setup can be folded by placing a mirror between the second and the third prism. Varying the prism insertion into the beam allows tuning of the amount of material dispersion introduced by the prism material. This material dispersion comes in addition to the negative GDD provided through angular dispersion. The overall GDD can thus be adjusted over an entire range from negative to positive values without any impact on the output beam pointing. The higher order dispersion introduced by a prism compressor limits its use to pulses longer than ~ 10 fs. Combining it with other dispersion compensation schemes for the (partial) compensation

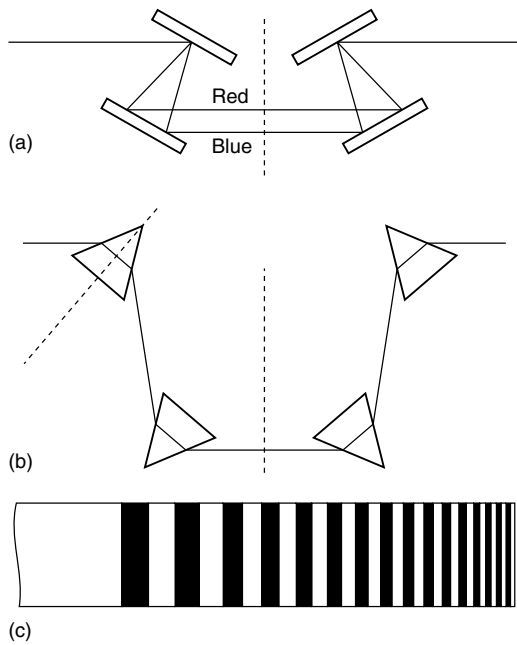


Figure 2 Common dispersion compensation schemes for the femtosecond domain: (a) grating compressor, (b) prism compressor, and (c) chirped mirror. The dashed lines indicate mirror symmetries within the setup. The grating compressor and the prism compressor can be folded by placing a mirror at the position of the vertical dashed line. For the wavelength fulfilling the Brewster condition, the beam path in the prism compressor is symmetric with respect to each of the prisms.

of higher order terms, extends its operation range into the few-femtosecond domain.

Chirped mirrors provide a very compact and flexible means of dispersion compensation (Szipöcs *et al.* 1994, Kärtner *et al.* 1997). They are manufactured by vacuum deposition of dielectric layer pairs onto a substrate. The thicknesses of the layer pairs are varied such that the Bragg condition for maximum reflection efficiency becomes a function of penetration depth into the coating structure. Typically, layer thicknesses are monotonically increasing. As a consequence, shorter wavelengths are reflected earlier in the mirror structure while longer wavelengths penetrate deeper. Negative GDD results from the longer optical path lengths experienced by increasingly longer wavelengths. The exact dispersion curve of a mirror structure can be custom tailored within a wide range using thin-film design methods. The bandwidth that can be achieved with chirped mirrors is sufficient to support few-cycle pulses. A typical chirped mirror designed for a Ti:sapphire laser operated at 800-nm wavelength can provide a GDD of about -50 fs^2 over a bandwidth larger than 300 nm. The maximum dispersion compensation available from chirped mirrors is limited by the total coating thickness that can be manufactured. Therefore, multiple reflections are normally required.

2.1.2 Self-phase Modulation

If the intensity of an ultrashort pulse becomes sufficiently high, optical materials do not respond linearly anymore to the incoming light field. The refractive index now not only depends on frequency, but also becomes a function of intensity. In lowest order, such an effect can be described by

$$n(I) = n_0 + n_2 I \quad (3)$$

where n_0 is the linear optical refractive index, I is the intensity, and n_2 denotes the nonlinear refractive index coefficient. This intensity dependence of the refractive index is referred to as the *optical Kerr effect*. For fused silica glass $n_2 \approx 2.5 \times 10^{-16} \text{ cm}^2 \text{ W}^{-1}$ when measured at 1- μm wavelength. This is a typical order of magnitude for many transparent materials in the visible to near-infrared spectral region. If we now let a pulse propagate through a medium of length L , it experiences a phase shift $\varphi(t) = -kn(I)L$. The nonlinear optical contribution $\varphi_2(t)$ to this phase shift can be written as

$$\varphi_2(t) = -kn_2 I(t)L = -\delta I(t) \quad (4)$$

The action of the pulse on its own phase through the optical Kerr effect is called *SPM*, and $\delta := kn_2 L$ is called the *SPM-coefficient*. The instantaneous oscillation frequency of a pulse is given by the first time derivative of its phase: $\omega(t) = d\varphi/dt$. As a consequence, SPM induces a nonlinear frequency shift

$$\omega_2(t) = \frac{d\varphi_2(t)}{dt} = -\delta \frac{dI(t)}{dt} \quad (5)$$

If an initially unchirped pulse (i.e., $\omega(t) = \omega_0$) enters the nonlinear optical medium, a positive SPM-coefficient will result in a red shift of the frequencies in the leading part of the pulse and a blue shift in its trailing wing (n_2 and thereby δ are positive for most materials in the visible and near-infrared). This situation is depicted in Figure 3. Pure SPM in the absence of dispersion does not modify the temporal shape of the pulse, but only its spectral content. A transform-limited pulse will always experience spectral broadening under such conditions. It should be noted that for certain combinations of dispersion and SPM, a pulse may also undergo spectral narrowing.

With the refractive index depending on intensity, the spatial beam profile will experience a transversely dependent nonlinear phase shift. In analogy to the temporal nonlinear phase shift, this phase shift is directly proportional to the beam intensity profile, i.e., a Gaussian beam creates a Gaussian nonlinear phase shift. For Gaussian or other bell-shaped intensity profiles, this phase shift results in a focusing effect on the beam. This

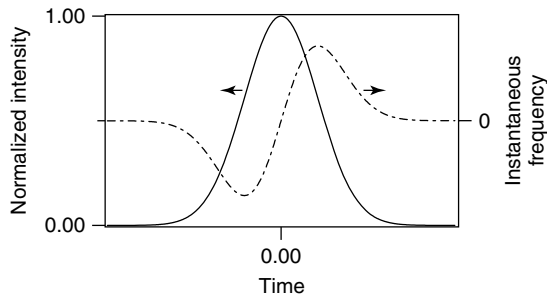


Figure 3 Spectral broadening of an initially unchirped pulse as a result of SPM. The temporal intensity profile of the pulse is shown as a solid line, its instantaneous oscillation frequency as a dash-dotted line. As a result of SPM with positive n_2 , frequencies on the leading edge of the pulse become red-shifted, those on the trailing edge get blue-shifted.

effect is referred to as *self-focusing*—the spatial analog to SPM.

2.1.3 Gain and Loss

Optical gain and loss change the energy contained within a pulse. Optical amplifiers of any type can provide gain, while loss may be due to various processes such as absorption, reflection, diffraction, or scattering. The amplitude of the pulse changes with passage through a gain medium according to $E_{\text{out}} = e^{gL_g} E_{\text{in}}$, where g is the gain coefficient per unit length and L_g the length of the medium. However, pulse energy cannot rise arbitrarily high due to energy conservation. Optical gain will therefore always saturate with increasing intensity. In the simplest case, but reasonably approximating many practical systems, the saturation behavior follows

$$g(I) = \frac{g_0}{1 + 2I/I_{\text{sat}}} \quad (6)$$

Here, g_0 represents the small-signal (or unsaturated) gain and I_{sat} is the saturation intensity. The saturation intensity depends only on photon energy and material constants.

Optical loss, on the other hand, exists in nonsaturable and saturable flavors. Reflection losses are an example for nonsaturable and therefore intensity-independent losses (at least below the damage threshold), whereas absorption losses can be saturated through depletion of the ground state of the absorbing transition. The action of saturable loss on a pulse is referred to as *self-amplitude modulation (SAM)*. Continuous loss mechanisms are described analogously to gain by replacing the gain coefficient with a loss coefficient l (per unit length) and adding a negative sign in front of the exponent: $E_{\text{out}} = e^{-lL_l} E_{\text{in}}$ (L_l is the length of the lossy medium). Simple absorbers follow the same saturation behavior described by equation (6) with g_0 replaced by the unsaturated losses l_0 and $g(I)$ replaced by $l(I)$.

2.2 Laser Oscillators

An ultrashort pulse laser oscillator, also referred to as an *ultrafast laser oscillator*, is the experimental prerequisite for any kind of time-resolved spectroscopy setup. Two fundamentally different pulse generation methods can be distinguished in the case of oscillators: Q-switching and modelocking. With Q-switching, pulse durations are always longer than the cavity round-trip time, i.e., the time taken by a laser beam to travel once through the entire cavity and back to the initial starting point. Q-switched pulse durations are typically in the microsecond to >10-ps range, while pulse repetition rates reach from anywhere in the low hertz to a few megahertz. Q-switching is the method of choice if high pulse energies from the oscillator are the main concern for a particular application.

In the modelocked case, pulses are always shorter than the cavity round-trip time. Usually, a single pulse is found within the cavity at any given moment. Typical modelocked oscillators produce pulses in the range of picoseconds to femtoseconds with pulse energies in the range of nanojoules to a few microjoules and pulse repetition rates from megahertz to gigahertz. Both Q-switching and modelocking come in an active and passive flavor, depending on the choice of the pulse-generating device. Because we focus our discussion on the femtosecond domain, we consider only passive modelocking in more detail. The femtosecond regime is not accessible through other methods. An up-to-date and exhaustive presentation of ultrafast solid-state laser technology covering Q-switching and modelocking in a wide variety of different laser materials is given by Keller (2007).

2.2.1 Passive Modelocking

Figure 4 shows an idealized passively modelocked laser. It consists of a gain material and a saturable loss modulator in between a high reflector and an output coupler forming the end mirrors of the resonator. One pulse travels back and forth between the two end mirrors. A small fraction of the beam leaves the cavity every time the pulse is reflected at the output coupler. The pulse round-trip time (the inverse of the repetition rate) is therefore given by the average intra-cavity group velocity v_g and the laser cavity length L through $T_R = 2L/v_g$. Higher repetition rates are realized by reducing the size of the laser. Under steady-state conditions, the output beam consists of an evenly spaced train of identical pulses. In the spectral domain, this translates into a comb of equidistant frequency lines. The relation between time and frequency domain for a train of modelocked pulses is depicted in Figure 5.

How is pulse formation taking place in the laser and how is pulsed operation stabilized against continuous (“cw”)

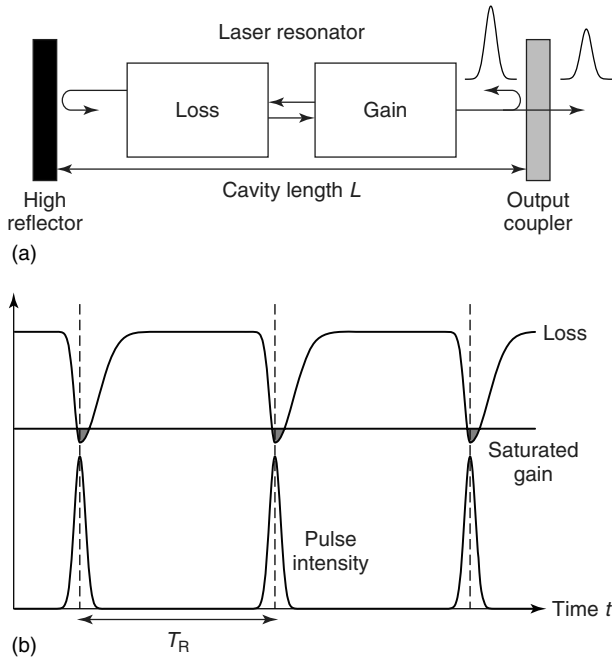


Figure 4 Schematic operation principle of a passively mode-locked laser. The idealized laser resonator shown in (a) contains the gain material and a saturable loss mechanism. The corresponding dynamics taking place in the resonator is depicted in (b). The saturable loss gets saturated dynamically while the gain is saturated by the time-averaged intensity only. This allows for a net gain window to open for intense pulses capable of sufficiently saturating the losses.

laser emission? The latter is illustrated in Figure 4(b). In a typical solid-state laser, the gain is saturated only by the average intra-cavity intensity and can therefore be assumed as constant over a single pulse. If the pulses are intense enough and the saturable loss modulator is fast enough, the pulses can open up a short net gain window over their duration. Any lower intensity radiation in the cavity experiences more loss than gain and therefore dies away quickly. As a consequence, pulsed operation is energetically favored over continuous operation. Modelocked dye, color-center, and semiconductor lasers show dynamical gain saturation, but the final outcome is similar to the case discussed above: pulsed operation is stabilized through short net gain windows around the actual pulses. In both cases, modelocking starts from intracavity intensity fluctuations. As soon as a noise spike is sufficiently high to saturate the losses, it is amplified and asymptotically forms into the steady-state pulse.

One needs to distinguish between slow and fast saturable loss modulators. Fast loss modulators have a response and recovery time on the order of the steady-state pulse duration, while slow loss modulators take a considerably longer time to recover from saturation. Stable modelocking with dynamical gain saturation requires saturable loss with

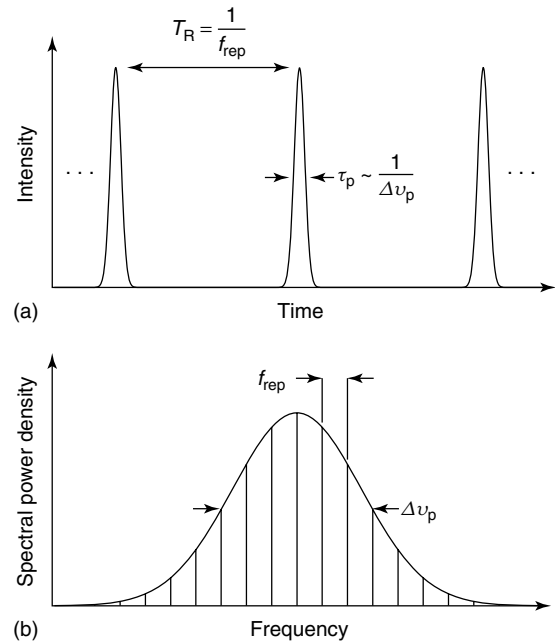


Figure 5 Time and spectral domain representation of a mode-locked pulse train. In the time domain shown in (a), the pulse train consists of an infinite sequence of identical pulses separated by the cavity round-trip time T_R . In the spectral domain depicted in (b), this translates into an equidistant comb of frequency lines separated by the pulse repetition rate f_{rep} . The spectral envelope is the Fourier transform of an individual pulse in the time domain. The FWHM pulse duration τ_p is inversely proportional to the spectral width $\Delta\nu_p$ due to this Fourier relationship.

a recovery time faster than the gain recovery time. In the static gain case relevant for solid-state lasers, pulse formation can be stabilized using a fast loss modulator. The most established mechanism for fast loss modulation is Kerr-lens modelocking (KLM, (Spence *et al.* 1991, Keller *et al.* 1991)). It makes use of self focusing in the gain material through the Kerr effect. Self focusing of the intense pulses modifies the pulsed beam compared to a low-intensity beam incapable of inducing a significant Kerr effect. With proper cavity design, the modified laser mode results in the pulsed beam experiencing more net gain than the low-intensity counterpart. KLM is the method of choice for the generation of the shortest pulses from laser oscillators and is most frequently used in Ti:sapphire oscillators (*see* Section 2.2.3).

However, it is also possible to obtain stable and robust pulse formation with statically saturated solid-state gain materials using a slow saturable loss mechanism. Intuitively, one might think that the net gain window remaining open after the trailing edge of the pulse destabilizes the pulse. In the femtosecond regime, pulsed operation can be stabilized in such a laser through soliton formation. Solitons are steady-state pulse shapes that are formed through

the interaction of net negative GDD and positive SPM. This interplay prevents dispersive broadening of the soliton in the cavity. Lower intensity background noise (“continuum”) in the laser does induce no or less SPM and therefore does not benefit from well-balanced SPM and GDD. Over many round-trips, the continuum therefore dispersively broadens, thereby spreading outside the net gain window opened by the soliton. Once outside of the gain window, the continuum is suppressed by the unsaturated losses. This modelocking technique is referred to as *soliton modelocking* (Kärtner and Keller 1995, Kärtner *et al.* 1996). The resulting pulses possess a hyperbolic secant shape and can be 10 to 30 times shorter than the absorber recovery time.

Saturable loss modulation is most commonly obtained via saturable absorption. The most successful saturable absorber for modelocking solid-state lasers is the semiconductor saturable absorber mirror (SESAM) structure (Keller *et al.* 1992, 1996, Keller 2003). It is often used in combination with the soliton modelocking method. In fact, the acronym SESAM describes an entire class of devices that have in common that a semiconductor saturable absorber is integrated into a mirror structure. Saturation of the absorber by intense pulses then leads to a reflectivity increase of the entire mirror structure. Such a SESAM device is manufactured using thin-film growth processes and offers a wide range of parameter engineerability. The engineerability is a consequence of the degrees of freedom in thin-film design and material choice. The most important parameters that characterize a SESAM besides operation wavelength are its recovery time, saturation fluence, modulation depth (i.e., maximum reflectivity change upon saturation), and nonsaturable losses (i.e., losses that remain even when the absorber is fully saturated). The semiconductor absorber is usually a semiconductor nanostructure: most commonly one or more quantum wells, but quantum dots have also been used for the absorber part (Lorenser *et al.* 2004). This allows tuning the absorber to the emission wavelength of the laser material. Recovery time can be controlled via the inclusion of defects into the semiconductor. Saturation fluence and modulation depth can be designed via the number and placement of the absorber layers within the multilayer structure and the optional addition of partially reflecting top layers. Nonsaturable losses may limit the laser efficiency for low gain lasers, which are influenced by the quality of thin-film growth and the reflectivity of the bottom mirror structure.

For the very common near-infrared solid-state lasers around a wavelength of 1 μm , the bottom mirror structure of the SESAM is an AlAs/GaAs Bragg reflector. The absorber is made of $\text{In}_x\text{Ga}_{1-x}\text{As}$ with the indium content x adjusted to obtain the desired band gap. The entire structure is grown using low-temperature molecular beam epitaxy. This particular choice of growth method results in low strain but

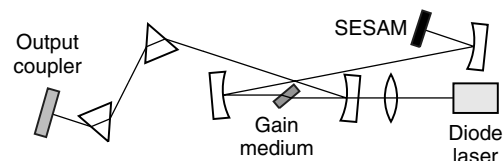


Figure 6 Typical cavity layout of a SESAM modelocked solid-state laser. A pair of prisms is used to achieve the net negative intra-cavity GDD required for soliton modelocking. A curved mirror focuses the laser mode onto the SESAM to obtain the flux levels required for the saturation of the absorber under the expected operating conditions.

relatively high defect densities. The latter is advantageous because it has a favorable effect on the recovery time of the device. The fastest and most important time constant of the SESAM recovery is due to intraband thermalization of the excited electrons and usually lasts on the order of 100 fs. Saturation fluences are typically in the range of 10–100 $\mu\text{J cm}^{-2}$. A modulation depth of $\sim 1\%$ is sufficient for stable passive modelocking of the most common 1- μm lasers, while nonsaturable losses of modern SESAM devices are usually negligibly small in this case. More information on the design and application of SESAMs for various laser parameters can be found in Keller (1999, 2007).

2.2.2 SESAM Modelocked Lasers at 1 μm Wavelength

Femtosecond optical pulses around 1- μm wavelength can be obtained from solid-state lasers using Nd^{3+} -doped glasses, Yb^{3+} -doped glasses, or Yb^{3+} -doped crystalline host materials as the active laser medium. Only these materials offer sufficient amplification bandwidth to support femtosecond operation. In these lasers, soliton modelocking is usually used as the modelocking mechanism in the femtosecond domain. A typical cavity layout of such a laser is shown in Figure 6. Intra-cavity dispersion compensation provides the necessary net negative GDD. The SESAM starts and stabilizes modelocking. The laser is pumped by high-brightness diode lasers, which is a considerable advantage in terms of efficiency, compactness, and cost compared to other pump schemes.

Table 1 lists a small selection of Nd^{3+} - and Yb^{3+} -doped laser materials and corresponding performance results. A more extensive list of laser materials and demonstrated performance can be found in (Keller 2007). In particular, the Yb^{3+} -based materials with crystalline hosts seem to be a very promising route toward high-energy femtosecond pulses directly from oscillators. Pulse energies above 10 μJ and average powers of tens of watts have already been demonstrated (Marchese *et al.* 2008, Südmeyer *et al.* 2008).

Table 1 Selection of femtosecond rare-earth doped-laser materials and demonstrated performance results

Laser material	Center wavelength (μm)	Pulse duration (fs)	Average power (W)	Repetition rate (MHz)	References
Nd:phosphate glass	1.054	275	1.4	74	(Paschotta <i>et al.</i> 2000)
Nd:fluorophosphate glass	1.065	60	0.084	114	(Aus der Au <i>et al.</i> 1997)
Yb:phosphate glass	1.025–1.065	58	0.065	112	(Hönninger <i>et al.</i> 1998)
Yb:YAG	1.03	340	0.17		(Hönninger <i>et al.</i> 1999)
		705	80	57	(Brunner <i>et al.</i> 2004)
		791	45	4	(Marchese <i>et al.</i> 2008)
Yb:KGW	1.037	100	0.126		(Paunescu <i>et al.</i> 2004)
	1.040	433	10	45	(Holtom 2006)
Yb:KYW	1.046	101	0.1	95	(Klopp <i>et al.</i> 2002)
	1.028	240	22	25	(Brunner <i>et al.</i> 2002)

The high average powers are made possible by the thin-disk laser head design that limits the detrimental impact of thermal load (Giesen *et al.* 1994). Further pulse energy scaling into the 100- μJ range with a few megahertz pulse repetition rate seems feasible in the near future.

2.2.3 Kerr-lens Modelocked Ti:Sapphire Oscillators

The shortest pulses from oscillators are nowadays produced with Ti^{3+} -doped sapphire (Ti:sapphire) lasers. The laser transition in Ti:sapphire is strongly phonon broadened resulting in a gain spectrum ranging from about 650 nm to well beyond 1000 nm with a gain maximum at about 780 nm. The spectrum of the generated pulses can extend even further by exploiting significant SPM in the sapphire crystal. Ti:sapphire lasers are pumped in the green to blue-green spectral region today mainly by frequency doubled solid-state lasers. The only modelocking mechanism that still works below pulse durations of about 30 fs is KLM. This is, therefore, the standard modelocking technique for Ti:sapphire lasers. Because KLM is not self starting, SESAMs or other loss modulators can be used in addition to initiate the modelocking process (Sutter *et al.* 2000, Steinmeyer *et al.* 1999). The broad bandwidth of Ti:sapphire oscillators is usually exploited for the production of either widely tunable longer (tens of femtosecond) pulses or extremely short pulses. The shortest pulse duration demonstrated so far is well below 5 fs (Rausch *et al.* 2008), which corresponds to less than two oscillation cycles at the carrier frequency. The output power of this particular laser was 90 mW at a repetition rate of 80 MHz. Ti:sapphire oscillators in general can provide output power levels of hundreds of milliwatts to above 1 W with several watts of pump power. Chirped mirrors are used for dispersion compensation because their large bandwidth and accurate control of higher order dispersion terms are required for the short pulse durations supported by Ti:sapphire lasers. The large bandwidth, strong nonlinearities, and higher order dispersion in the sub-10-fs pulse duration regime lead to more

complicated spectral and temporal shapes of the emitted pulses. Pulse shapes are not as clean as those generated by soliton modelocked lasers operating at longer pulse durations. Small pre and postpulses are common for sub-10-fs pulses.

2.2.4 Other Femtosecond Oscillator Technologies

Besides the examples given above, a wide range of other femtosecond oscillator technologies exist. An overview of solid-state laser technology can be found in Keller (2007). Oscillators based on optical fibers are described in Fermann *et al.* (1997). At spectral locations that are difficult to reach, dye lasers are still being used for time-resolved spectroscopy applications, while optical parametric oscillators offer yet another way of generating femtosecond pulses in spectral regions that are not covered by solid-state lasers, in particular, the visible and some regions in the infrared (*see e.g.*, (Byer and Piskarskas 1993, Bosenberg and Eckhardt 1995)).

Typical output pulse energies of most oscillators are on the order of nanojoules. If higher energies are needed at oscillator repetition rates, extended cavities can be used. By increasing the length of the laser cavity and keeping the average power constant, the repetition rate drops and pulse energy rises. This approach was for example chosen in the demonstration of $>10\text{-}\mu\text{J}$ pulses from an Yb:YAG thin-disk oscillator (Marchese *et al.* 2008). Another way to increase the effective pulse energy at the full repetition rate of the oscillator is to send the output beam into an external enhancement cavity. If the length of this additional cavity is perfectly locked electronically to the length of the oscillator, pulses from several consecutive round-trips can interfere constructively, thereby building up energy. The maximum build-up factor is limited by the achievable finesse of the external cavity. This technique has been applied for the generation of high-order harmonics with a Ti:sapphire oscillator (Jones *et al.* 2005). At somewhat

reduced repetition rates (e.g., 1 MHz compared to the full 100 MHz of an oscillator), cavity dumping can be used to obtain higher pulse energies. This technique relies on the fact that the pulse energy inside the modelocked laser can be much higher than that in the output beam, and inversely proportional to the output coupling percentage (e.g., for a laser with 4% output coupling, intra-cavity pulse energy would be 25 times the energy of the output pulses). A fast optical modulator is used to switch the output coupling fraction from a very low value to almost 100% every couple of round-trips. The electronic control over the output coupling also allows for variable repetition rates. With cavity-dumped oscillators, pulse energies of hundreds of nanojoules or even microjoules and peak powers of several megawatts at up to megahertz repetition rates can be achieved. An example and additional references can be found in Pshenichnikov *et al.* (1994). If even higher pulse energies or peak powers are required, additional amplification of the oscillator pulses becomes necessary.

2.3 Amplifiers

Amplification of femtosecond pulses to significant energies has been made possible only through a technique known as *chirped-pulse amplification (CPA)* (Perry and Mourou 1994). Before the invention of CPA, amplifiers were limited by the onset of spatial and temporal pulse distortions through self focusing and SPM and eventually optical damage to the amplifier medium as a result of the high peak powers. CPA circumvents this problem by temporally stretching the femtosecond pulses from the oscillator by orders of magnitude. The energy of such a long pulse can then be safely amplified without reaching critical peak powers. A compressor providing the opposite sign of dispersion compared to the stretcher then recompresses the

amplified pulse down to its femtosecond transform-limited duration. The temporal recompression of the amplified pulses leads to orders of magnitude increase in peak power. The CPA method is schematically depicted in Figure 7.

The stretcher most commonly provides positive dispersion. In the simplest case (for sufficiently short pulses and low amplification levels), it is just a piece of dispersive material. Often, it is an arrangement of two gratings and a telescope, possibly folded in the middle of the telescope (Martinez 1987). Ideally, the compressor is perfectly matched to the stretcher, allowing compensation of higher order dispersion from the stretcher. With CPA, amplifiers are not peak power limited anymore but are usually average power limited. The repetition rate of amplifiers is well below that of oscillators—typically in the kilohertz regime or below. Owing to the average power limitation, higher pulse energies mean lower repetition rates. Pulse durations down to about 20 fs can be obtained at pulse energies on the order of 1 mJ. With multiple amplification stages, pulse energies well beyond 1 J (even beyond the kilojoule level in extreme cases) are possible at the expense of longer pulses. The main limiting factors on pulse duration are the effect of gain narrowing, imperfect higher order dispersion compensation, and the bandwidth of the grating-based stretcher and compressor. Gain narrowing is caused by the fact that spectral components of the pulse located around the gain maximum of the amplification medium experience more gain than the spectral wings of the pulse. Thereby, the pulse bandwidth is effectively reduced as a direct consequence of the amplification process. This also explains why higher pulse energies usually come along with longer pulses. Methods for compressing the amplified pulses to shorter durations are discussed in Section 2.6.

To extract most of the energy stored in the gain medium, usually more than one passage through the medium is

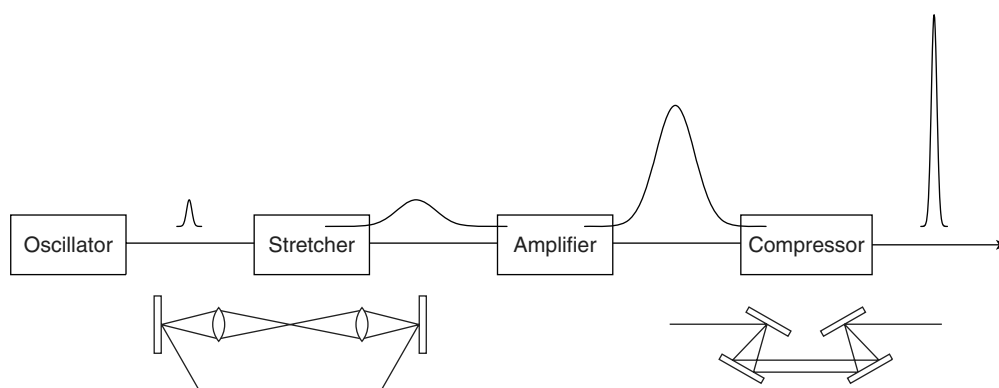


Figure 7 Operation principle of chirped-pulse amplification. The short output pulse from a modelocked oscillator is temporally stretched by several orders of magnitude. This allows for safe amplification. After amplification, the pulses are recompressed to their transform limit, thereby gaining orders of magnitude in peak power. The experimental setup of stretcher and compressor are sketched schematically.

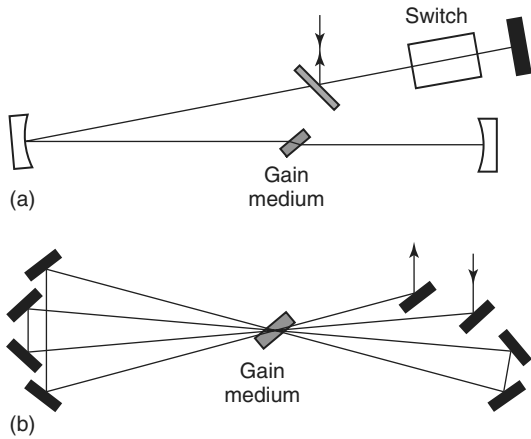


Figure 8 Basic amplifier geometries: (a) regenerative amplifier and (b) multipass amplifier.

required. This multiple passage is realized with two fundamentally different amplifier geometries shown in Figure 8. A regenerative amplifier consists of a cavity with a fast optical switch. The switch opens to allow the oscillator pulse to enter the cavity. The pulse then circulates several times back and forth. After the desired number of passes through the amplifier medium, the switch opens again and releases the amplified pulse. The other amplifier geometry is referred to as *multipass amplifier*. Here, the beam is folded in such a way that it passes the gain medium several times under different angles. The parameter range that can be covered with these two geometries overlaps over a wide range. Generally, it can be said that due to the cavity confinement, regenerative amplifiers offer better beam quality, while multipass amplifiers allow the production of shorter pulses and are scalable to higher energies.

2.4 Carrier-envelope Offset Phase and Frequency Combs

In Section 2.2.1, we introduced the fact that a modelocked oscillator produces an evenly spaced train of pulses separated by the cavity round-trip time T_R . The spectral domain equivalent to this is a comb of narrow frequency lines spaced by the pulse repetition rate $f_{\text{rep}} = 1/T_R$ and with an envelope given by the spectrum of an individual pulse (Figure 5). In this paragraph, we further refine this picture. A closer examination at the electric-field envelope and the underlying carrier wave reveals that there is a phase slippage between the carrier and envelope when comparing consecutive pulses in the pulse train. This situation is sketched in Figure 9(a). This slippage or offset is a consequence of the difference between group and phase velocity in the oscillator cavity. The electric-field envelope circulates at group velocity, while the carrier wave propagates

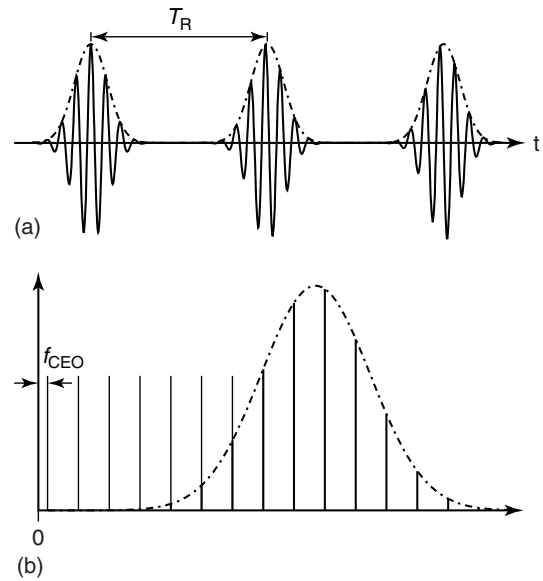


Figure 9 Effect of carrier-envelope offset in time and frequency domain. (a) The relative phase between the carrier wave and the electric-field envelope changes by $\Delta\varphi_{\text{CEO}}$ from pulse to pulse in the pulse train. (b) The rate of phase change (i.e., phase change per cavity round-trip time T_R) leads to a zero-offset f_{CEO} of the frequency comb representing the pulse train in frequency domain.

at phase velocity. The resulting phase offset is referred to as CEP $\Delta\varphi_{\text{CEO}}$. In the absence of external perturbations, the CEP remains constant between any consecutive pulses of the entire pulse train. This means that the rate of phase change remains constant. This rate can be expressed as

$$f_{\text{CEO}} = \frac{1}{2\pi} \frac{\Delta\varphi_{\text{CEO}}}{T_R} \quad (7)$$

It manifests itself as an offset of the frequency comb from zero frequency as shown in Figure 9(b). The positions of the frequency lines in the comb are therefore given by

$$f_m = m f_{\text{rep}} + f_{\text{CEO}} \quad (8)$$

where m is an integer number.

There are two main classes of applications for which all this is relevant. One class of applications relies on the exact knowledge and control of the positions of the comb lines in frequency domain. The second set of applications requires control of the position of the carrier oscillations with respect to the electric-field envelope in time domain. In both scenarios, f_{CEO} needs to be measured, controlled, and stabilized. Measurement of f_{CEO} can be done in several ways as outlined by Telle *et al.* (1999). The most successful approach is the so-called f -to- $2f$ method. This technique relies on the pulses covering an octave-wide spectral range—either directly from the laser or after spectral broadening through SPM. The pulse train is then

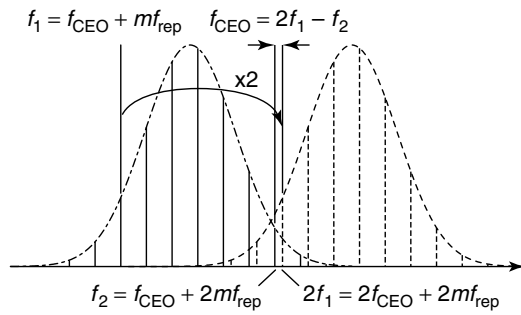


Figure 10 f -to- $2f$ scheme for measuring and locking the carrier-envelope offset frequency f_{CEO} . For octave-spanning spectra, the high-frequency side of the frequency comb (solid comb lines) overlaps with the low-frequency side of its second harmonic (dashed comb lines). The beat note between the frequency-doubled comb line originating from the low-frequency side and the neighboring comb line from the high-frequency side of the fundamental pulse train corresponds to f_{CEO} .

focused into a second harmonic generation (SHG) crystal. This produces a frequency-doubled version of each comb line of the original frequency comb. Owing to the large spectral coverage of the pulses, the lowest lying parts of the frequency-doubled spectrum overlap with the highest frequency parts of the fundamental spectrum. While the fundamental comb line positions are given by equation (8), their frequency-doubled versions are given by $f_m^{\text{SHG}} = 2f_m = 2mf_{\text{rep}} + 2f_{\text{CEO}}$. Sending the overlapping spectral region onto a fast photo-diode we can thus produce a beat note at $f_{\text{CEO}} = f_{2m} - f_m^{\text{SHG}}$. This scheme is visualized in Figure 10. The individual comb lines lie in the optical frequency range and therefore cannot be detected with a photo-diode. However, the beat note f_{CEO} is always anywhere between 0 Hz and f_{rep} . It is thus located in the electronically accessible microwave range.

We can control f_{CEO} by slightly modifying the intracavity balance of group and phase delay. The most common way to achieve this is by applying a small power modulation to the pump source of the oscillator (Baltuska *et al.* 2003). The perturbations caused by the power modulations induce changes in the f_{CEO} value. These changes can be tracked with the f -to- $2f$ method and f_{CEO} can be locked to a desired value by closing this feedback loop. f_{CEO} is stabilized against other perturbations of the oscillator by locking it to a stable microwave reference frequency. For certain applications only the ratio between f_{CEO} and f_{rep} needs to be stable. The carrier-envelope offset frequency is then locked to the desired fraction of f_{rep} , which is obtained by electronically dividing the repetition rate recorded by a fast photo-diode.

If it is the CEP $\Delta\varphi_{\text{CEO}}$ that matters for a given application, additional compensation for fluctuations (e.g., thermal drift) in the setup is required. This is the case when

CEP-stable pulses are needed after further amplification. In this scenario, one tracks changes of $\Delta\varphi_{\text{CEO}}$ by overlapping the amplified pulses with their second harmonic in a spectrometer. For this method to work, the pulses need to cover a frequency range of at least one octave. If such bandwidth is not available to begin with, this is typically achieved by spectrally broadening the pulses through SPM in a sapphire plate. In the region of spectral overlap, one will observe interferences that are proportional to $\cos(\omega\tau + \Delta\varphi_{\text{CEO}})$, where τ is a possible time delay between the fundamental and the second-harmonic pulse. Any change in CEP therefore manifests itself through a shift in the spectral interference fringes. The CEP can be stabilized against fluctuations in the setup by feeding an additional error signal proportional to the fringe-shift back into the f -to- $2f$ feedback loop of the oscillator. The oscillator thereby precompensates drift and slow fluctuations in the amplifier. More details on how to extract the drift of $\Delta\varphi_{\text{CEO}}$ from the spectral interferences can be found in Section 3.1.2 on spectral interferometry. A good description of the nested feedback loops is given by Baltuska *et al.* (2003). Fully passive stabilization of $\Delta\varphi_{\text{CEO}}$ is possible by using optical difference-frequency mixing as it can be found in certain optical parametric amplifier (OPA) configurations (Baltuska *et al.* 2002).

Stabilized optical frequency combs find an important application in precision frequency metrology. An unknown optical frequency can be precisely measured by recording and electronically counting the beat note between that frequency and a known line of a well-characterized frequency comb. When locking the oscillator repetition rate (i.e., comb spacing) to the microwave standard of time even absolute measurements of optical frequencies are possible with accuracies of 16 or more digits. The modelocked oscillator then serves as clockwork transferring the microwave frequencies of the Cs atomic clock into the optical domain. This particular application of frequency combs forms an important part of the 2005 Nobel Prize in Physics by Theodor W. Hänsch and John L. Hall (Hänsch 2006). For more information on frequency combs in the VUV (*see* Eikema and Ubachs 2011: **Precision Laser Spectroscopy in the Extreme Ultraviolet**, this handbook).

Stabilization and control of the CEP is interesting for time domain applications when the process being studied strongly depends on the electric field of the pulse rather than its envelope. Significant effects can be expected if the pulses are sufficiently short and therefore contain only few optical oscillation cycles underneath the envelope. In a few-cycle pulse, the peak electric-field amplitude changes noticeably from half-cycle to half-cycle. The maximum electric-field strength that is reached depends on whether a field oscillation maximum coincides with the envelope maximum or not (Figure 9a) and

is therefore controllable through the CEP. In particular, highly nonlinear processes may exhibit a pronounced CEP dependence. An important application exploiting the CEP dependence in HHG is the production of isolated attosecond pulses. This example is discussed in detail in Section 4.1.2.

2.5 Parametric Amplifiers

For time-resolved spectroscopy in spectral regions not covered by conventional amplifier media, optical parametric sources often represent an excellent and sometimes the only choice. If an optical field drives a noncentrosymmetric transparent material sufficiently hard, its polarization contains a contribution that essentially splits a higher energy photon into two lower energy photons. Because energy conservation cannot be violated in this process, the three photons fulfill the condition

$$\hbar\omega_p = \hbar\omega_s + \hbar\omega_i \quad (9)$$

where ω_p is the frequency of the highest-energy photon driving the process, called the *pump photon*. The two other waves generated are referred to as *signal and idler* with their respective frequencies ω_s and ω_i following the convention $\omega_i < \omega_s < \omega_p$. At the degeneracy point $\omega_s = \omega_i = \omega_p/2$ is met. The parametric interaction is only efficient and macroscopically relevant if also momentum conservation is fulfilled:

$$\hbar\mathbf{k}_p = \hbar\mathbf{k}_s + \hbar\mathbf{k}_i \quad (10)$$

with \mathbf{k}_p , \mathbf{k}_s , and \mathbf{k}_i denoting the wave-vectors of pump, signal, and idler, respectively. Meeting this condition is called *phase matching*. The nonlinear optical effect splitting a pump photon into a signal and idler photon is called *optical parametric generation (OPG)*, which is also exploited in optical parametric oscillators. If a weak signal beam is seeding the process, this beam may experience significant amplification by converting a large fraction of the pump energy into signal and idler photons. The device is then referred to as *optical parametric amplifier*. With a sufficiently intense pump, OPAs can amplify the seed by many orders of magnitude in a single pass. Another advantage of OPAs besides the large gain and their flexibility with respect to generated wavelengths is the fact that no thermal load is put on the nonlinear medium during the parametric interaction.

Phase matching is classically achieved by exploiting the birefringence of the nonlinear medium. Generally, equation (10) can only be exactly fulfilled for one set of pump, signal, and idler wavelengths. However, the

mixing process can still be efficient for other wavelengths as long as

$$L_{\text{nlo}} < \frac{\pi}{|k_p - k_s - k_i|} \quad (11)$$

with L_{nlo} representing the length of the nonlinear optical medium. The right hand side of equation (11) is called *coherence length*. This condition indirectly defines the phase matching bandwidth for the parametric process. The phase-matching bandwidth is therefore primarily determined by the dispersion properties of the nonlinear medium. Particularly large bandwidths can be phase-matched if the group velocities of signal and idler can be matched.

Femtosecond OPAs are often pumped by Ti:sapphire amplifier systems at the fundamental wavelength of ~ 800 nm or the second harmonic at ~ 400 nm. The seed is typically obtained from the pump laser through white-light generation (SPM) in a sapphire plate. Pulse durations of the generated signal and idler pulses are usually in the tens to hundreds of femtoseconds. Pulse energies of such OPAs are in the microjoules range. A very popular nonlinear material for OPAs is beta barium borate (BBO). If it is pumped by the second harmonic of Ti:sapphire while pump and signal beams form an angle of 3.7° , group velocity matching of signal and idler and thereby an extremely large amplification bandwidth in the visible from about 500–750 nm is obtained. In this noncollinear OPA (NOPA) configuration, signal pulse durations around 5 fs have been demonstrated starting from ~ 100 fs pump pulses. BBO pumped by 800 nm allows covering wavelengths from 1.1 to $1.6 \mu\text{m}$ with the signal and $1.6\text{--}3 \mu\text{m}$ with the idler beam. Longer wavelengths can be generated with KTiOPO₄ (KTP), KNbO₃, or LiNbO₃. Generally, the spectral range accessible through OPAs is only limited by the dispersive properties of the medium and its transparency range.

The gain profile of an OPA is essentially determined by its dispersive properties. Therefore, almost flat-top gain curves can be found, significantly reducing the gain-narrowing effect compared to the Lorentzian or Gaussian profiles of conventional amplifier media. Together with the large gain and negligible thermal loads, this property renders OPAs ideal sources of energetic few-cycle pulses. If pump and signal are derived from the same oscillator, the idler wave is even automatically CEP stabilized (Baltuska *et al.* 2002). For the production of very intense pulses, such amplifiers are implemented using the CPA technique. Such systems are referred to as *optical parametric chirped-pulse amplifiers (OPCPA)*. The main difficulty of OPCPA sources lies in the fact that the parametric interaction takes place instantaneously. As opposed to a conventional gain material, an OPA does not store energy. Temporal overlap and timing jitter between pump and seed are therefore very critical.

An excellent and more detailed review of femtosecond OPA technology is given by Cerullo and Silvestri (2003).

2.6 External Pulse Compression

External pulse compression can be used if shorter pulses than those obtained directly from a particular laser or amplifier system are desired. All external pulse compression schemes share in common the generation of additional spectral content. This additional content is then compressed into a short pulse by applying dispersion compensation schemes to reach a flat spectral phase. Here, we limit the discussion to compression of intense pulses from amplifiers. In this scenario, the two most established techniques are hollow-core optical fiber compression (Nisoli *et al.* 1997) and compression based on optical filamentation (Hauri *et al.* 2004). Both methods yield similar typical pulse durations around 5 fs and pulse energies of hundreds of microjoules if driven by ~ 30 fs, < 1 mJ Ti:sapphire pulses. Pulse durations have even been pushed down into the region around 3 fs, the shortest pulses available in the visible to near-infrared spectral region. The main limitation on pulse duration comes from the accuracy and bandwidth of the dispersion compensation, not from the spectral bandwidth available from the hollow-core fiber or the filament.

In the hollow-core fiber technique, an amplified laser pulse is launched into a rare gas filled capillary. The mode of this hollow waveguide is guided over a length of typically 1 m and confined to a diameter of 200–300 μm . As rare gases, Ar or Ne at absolute pressures of several 100 mbar are used. Owing to the confinement and long interaction length in the waveguide, the launched pulses experience significant SPM even with the small nonlinearity of rare gases. SPM is the dominant spectral broadening mechanism in the hollow-core fiber approach.

Filamentation compression is performed by weakly focusing an intense pulse into a rare gas filled cell. Ar is the most commonly used gas at pressures of several hundred millibar. As a consequence of the Kerr effect, the pulse undergoes self-focusing. Once the intensity rises sufficiently high, the gas is ionized. The free electrons generated through ionization counter-act the self-focusing. The optical filament results from a dynamical equilibrium between self-focusing and plasma defocusing. The filament is maintained with a diameter on the order of 100 μm and over a length of tens of centimeters. Over this long interaction length, the pulse is spatially, spectrally, and temporally reshaped due to plasma interaction, SPM, self-steepening, and many other nonlinear processes. As a consequence of the non-negligible plasma contribution to the spectral broadening, the filament spectra show a larger blue shift compared to those from the hollow-core fiber. Under certain conditions, the complex nonlinear interaction in filamentation may yield temporally

self-compressed pulses. Furthermore, owing to the absence of a physically existing waveguide, filamentation holds the promise for scalability toward higher pulse energies. The hollow-core fiber method is limited to energies of about 1 mJ. Both, hollow-core fiber and filamentation compression have been shown to preserve the CEP stabilization of the input pulses. A detailed comparison of the two techniques is given by Gallmann *et al.* (2006).

3 FEMTOSECOND TECHNIQUES

The main challenge when performing time-resolved spectroscopy with femtosecond pulses stems from the fact that any detection electronics is slower than the optical pulses used in the experiment. Throughout the optical spectrum only time-integrating or energy detectors exist. One therefore needs to find ways to map the fast dynamics being studied to practically measurable quantities. The standard approach to solve this problem found in most ultrafast time-resolved experiments is sketched in Figure 11. One of two initially synchronized pulses is sent through a delay line of variable length Δx . The path length difference Δx translates into a time delay $\tau = \Delta x/c$. Because length differences can be measured very accurately, τ is known very accurately as well. The delayed pulse pair is then focused onto the sample under study. The first pulse triggers the process of interest, while the second pulse experiences the response of the sample induced by that process. The time-integrating detector records the impact of that response on the second pulse. This time-integrated signal is then recorded as a function of delay time τ . As a result, a time-resolved measurement is performed over many laser shots. Furthermore, it is implicitly assumed that the process being studied is repeatable and evolves in an—up to measurement accuracy—identical way whenever a pulse triggers it. The first pulse arriving at the sample is called the *pump*. The second pulse, the probe, is typically chosen much weaker than the pump such that it does not perturb

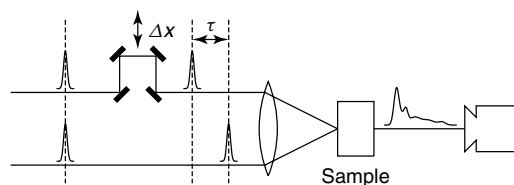


Figure 11 Pump-probe scheme for ultrafast time-resolved measurements. Two initially synchronized pulses are delayed with respect to each other through a variable delay line. The first pulse triggers the process to be studied, while the second pulse probes the response of the medium to that process. The output signal is recorded with a time-integrating detector as a function of delay time.

the system being studied. The entire scheme is generally referred to as *pump-probe scheme*. The achievable time-resolution is mainly limited by the pulse durations used in the experiment.

A simple example is the pump-probe measurement of the recovery time of a saturable absorber. The pump pulse saturates the absorption by depleting the ground state of the absorbing transition. Therefore, if the probe pulse follows the pump well within the recovery time of the absorber, it will not experience absorption. Before the pump pulse and at delays much larger than the recovery time, the probe pulse will be significantly absorbed. The recovery time can therefore be determined by recording the transmitted probe pulse energy as a function of delay time and monitoring the gradual reduction in transmission with increasing delay to the pump. The pump-probe idea can be extended to much more sophisticated schemes: more than two delayed pulses can be used, spectra instead of energy or changes in the polarization state can be recorded, etc. Many examples can be found elsewhere in this handbook (see Hamm 2011: **2D-Infrared Spectroscopy** and Frey *et al.* 2011: **High-resolution Rotational Raman Coherence Spectroscopy with Femtosecond Pulses**, this handbook). However, the basic principle remains the same and can even be transferred into the attosecond domain (see Wörner and Corkum 2011: **Attosecond Spectroscopy**, this handbook and Section 4.2).

3.1 Ultrashort Pulse Characterization

We have seen how ultrashort optical pulses can be used to temporally resolve dynamics in the femtosecond regime. But how does one measure the pulses themselves without requiring even shorter events to sample them? A variety of pulse characterization methods have been developed during the past decades that yield information about the temporal structure of femtosecond optical pulses. In this paragraph, we introduce several of the most important techniques. The discussion starts with the classical intensity and interferometric autocorrelation (IAC). These two methods reveal only limited information about the pulses. However, as easy to implement and easy to operate characterization tools they still find widespread use. We then introduce spectral interferometry. In a strict sense, spectral interferometry is not a pulse characterization method as it only measures spectral phase differences of an unknown pulse with respect to a well-characterized reference. It is, however, a very straightforward and sensitive method to measure these phase differences. On its own or in combination with another pulse characterization technique it can be a powerful tool for time-resolved spectroscopy. Full information on the amplitude and phase of femtosecond pulses

can be obtained with frequency-resolved optical gating (FROG) or spectral phase interferometry for direct electric-field reconstruction (SPIDER). FROG can be considered an extension of the classical autocorrelation methods, while SPIDER is a self-referenced version of spectral interferometry. Many other amplitude and phase characterization techniques exist, of which some could be attractive alternatives in special experimental scenarios. With FROG and SPIDER, we limit our discussion to the most established and most general approaches. We will further focus on the most common implementations of the two techniques. While pulse characterization of some sort forms part of every laboratory working with ultrashort optical pulses, the more advanced methods may also serve as spectroscopic tools. Measuring the amplitude and phase of a pulse before and after interaction with a sample allows extracting the response of the medium. Measuring the complex pulse shapes obtained in a coherent-control experiment based on feedback-optimization through a learning algorithm may reveal deeper insight into the system being studied. Pulse characterization techniques can be considered prototypes of time-resolved spectroscopy experiments. Their description in this paragraph should also provide a starting point for how time-resolved methods work and how such measurement schemes can be implemented.

3.1.1 Classical Methods

Possibly the simplest and oldest partial pulse characterization method is to measure the pulse spectrum with a spectrometer. Because this measurement does not contain any information about the spectral phase, the temporal structure of the pulse remains undetermined. The simplest techniques revealing some of the temporal structure of femtosecond pulses are intensity autocorrelation and IAC (Haus *et al.* 1975, Diels *et al.* 1978).

The experimental apparatus for the background-free intensity autocorrelation is shown in Figure 12(a). The beam enters a Michelson-interferometer-like arrangement, where it is split into two independently adjustable arms. The parallel, but noncollinear beams at the output are focused into a medium with instantaneous second-order nonlinearity. A second-order nonlinear material has a nonzero second-order dielectric susceptibility $\chi^{(2)}$. This nonlinear susceptibility gives rise to an electric field oscillating at the second harmonic of the input field. In our case, the input field consists of a superposition of the two pulse replicas. The generated second harmonic field $E^{(\text{SH})}(t)$ thus becomes

$$\begin{aligned} E^{(\text{SH})}(t) &\propto \chi^{(2)}(E(t) + E(t - \tau))^2 \\ &= \chi^{(2)}(E(t)^2 + 2E(t)E(t - \tau) + E(t - \tau)^2) \end{aligned} \quad (12)$$

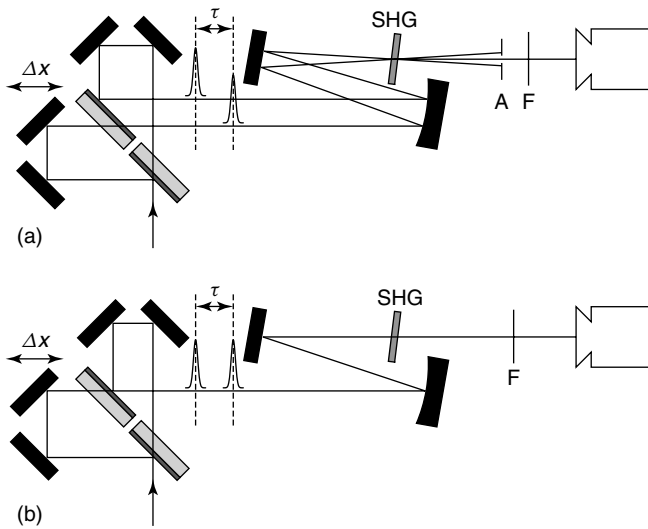


Figure 12 Autocorrelation setups. (a) Intensity autocorrelation and (b) interferometric autocorrelation. A spherical mirror focuses the beams into a second harmonic generation (SHG) crystal. A filter (F) removes residual light at the fundamental wavelength. The detector records photocurrent as a function of delay. In the intensity autocorrelation setup, an aperture (A) blocks the fundamental beams and their direct second harmonic. Only the beam created through mixing of the two beams reaches the detector.

where $E(t)$ is the electric field of the pulse to be characterized and τ represents the delay between the two pulse replicas. At the output of the nonlinear crystal, three beams corresponding to the three terms on the right-hand side of equation (12) are observed: The first and the third term represent the two directly frequency-doubled beams, while the second term is due to the mixing of the two noncollinear beams. Because of momentum conservation they are spatially separated from each other. The directly frequency-doubled beams are therefore easily suppressed with an aperture after the nonlinear medium. Usually, the residual fundamental radiation is filtered out in front of the detector to avoid spurious signals or even damage. Instead of SHG and linear detector, a two-photon absorbing photodiode can be used directly. The output current from the slow detector is proportional to the energy in the signal beam, which again is proportional to the integrated signal intensity. The recorded detector current as a function of delay $I_{ac}(\tau)$ thus becomes

$$\begin{aligned} I_{ac}(\tau) &\propto \int_{-\infty}^{\infty} |E(t)E(t-\tau)|^2 dt \\ &= \int_{-\infty}^{\infty} I(t)I(t-\tau) dt \end{aligned} \quad (13)$$

For some analytic pulse shapes, a simple relation between the width of the autocorrelation function and the width of

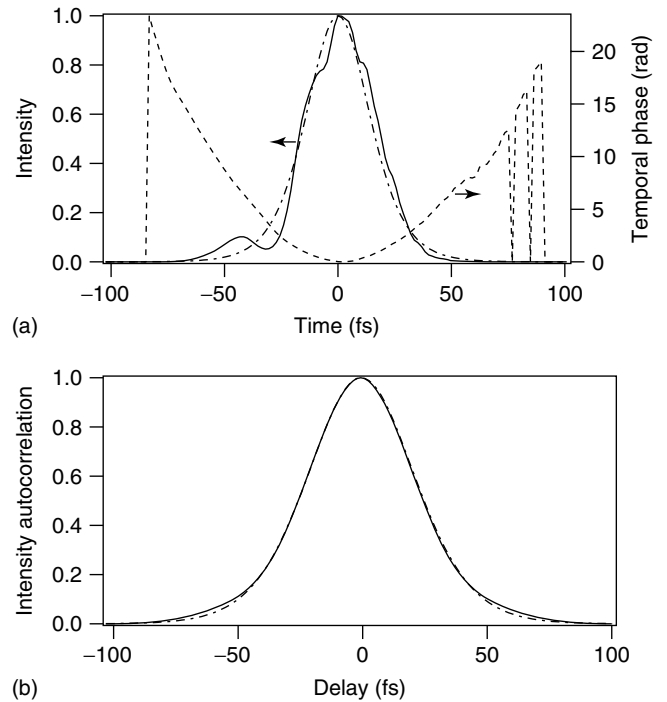


Figure 13 Pulse-shape insensitivity of the intensity autocorrelation. (a) The actual pulse shape measured with frequency-resolved optical gating (solid line) yields an autocorrelation trace that is very similar to that of an unchirped sech^2 pulse (dash-dotted line). For completeness, the temporal phase of the measured pulse is also shown (dashed line). (b) The solid autocorrelation trace corresponds to the strongly chirped measured pulse, the dash-dotted trace to the sech^2 pulse. In the presence of experimental noise, the two autocorrelation traces become indistinguishable.

the input pulse can be found. In all these cases, however, it is assumed that no or just a linear chirp is present on the pulse to be characterized. Because the autocorrelation function only depends on the pulse intensity, very limited information on the phase can be extracted. For example, assuming a linear chirp, the amount of chirp can be found by comparing the independently measured spectral bandwidth with the actually measured pulse duration. The sign of the chirp, however, remains undetermined because equation (13) is symmetric with respect to reversal of the direction of time.

The intensity autocorrelation is rather insensitive toward the pulse shape. This is demonstrated with actual experimental data in Figure 13. One should therefore restrict the application of intensity autocorrelation to cases in which the pulse shape is known a priori or in which only a rough estimate for the pulse duration is desired. Such a priori knowledge of the pulse shape is available, for example, if a passively modelocked laser is known to operate in the soliton-modelocking regime (Kärtner and Keller 1995, Kärtner *et al.* 1996).

A slight modification of the setup converts an intensity autocorrelator into an interferometric autocorrelator (Figure 12b) (Diels *et al.* 1978). This time the two pulse replicas interact collinearly in the nonlinear medium. As a result, the energy of the full nonlinear signal given in equation (12) is detected as a function of the delay τ . The detector thus records

$$I_{\text{iac}}(\tau) \propto \int_{-\infty}^{\infty} |(E(t) + E(t - \tau))^2|^2 dt \quad (14)$$

This equation is symmetric in its argument τ as it is the case for intensity autocorrelation. An ideal IAC possesses an 8:1 peak-to-background ratio independent of the input pulse shape.

The IAC contains more information than the intensity autocorrelation. Owing to the interference terms it also reveals some information about the phase of the pulse. In Figure 14 it is demonstrated that two pulses with identical temporal pulse shape but different spectral bandwidths can be distinguished by their IAC. This is not possible with intensity autocorrelation alone, where, for example, an additional spectral measurement would be required for this purpose. Additionally, the IAC is more sensitive to the pulse shape than its noninterferometric counterpart. Still, the pulse width is usually determined from the IAC by fitting the theoretically expected autocorrelation trace for a particular pulse shape to the experimental data. Very often a transform-limited pulse is assumed in this procedure. This limits the use of the IAC to estimating durations of near-transform-limited pulses and to the qualitative detection of the presence of chirp.

3.1.2 Spectral Interferometry

Strictly speaking, spectral interferometry is not a pulse characterization technique. It measures only the relative spectral phase within the spectral overlap region of two interfering pulses. Several reasons lead us to include this method in this paragraph nevertheless. First, spectral interferometry lies at the heart of the SPIDER pulse characterization method discussed in Section 3.1.4. Second, it can be used to measure very weak pulses by interfering them with a well-known and stronger reference pulse. And third, it is a sensitive tool to track spectral phase changes in time-resolved spectroscopy experiments and is therefore of definite interest within the scope of this article.

In spectral interferometry, a spectrally broadband beam is split into two. Along one path, the beam acquires a spectral phase $\varphi_1(\omega)$, whereas the other beam acquires $\varphi_2(\omega)$. At the end of both paths, the two beams are collinearly recombined and sent into a spectrometer. Obviously, the phase contributions acquired before splitting and after

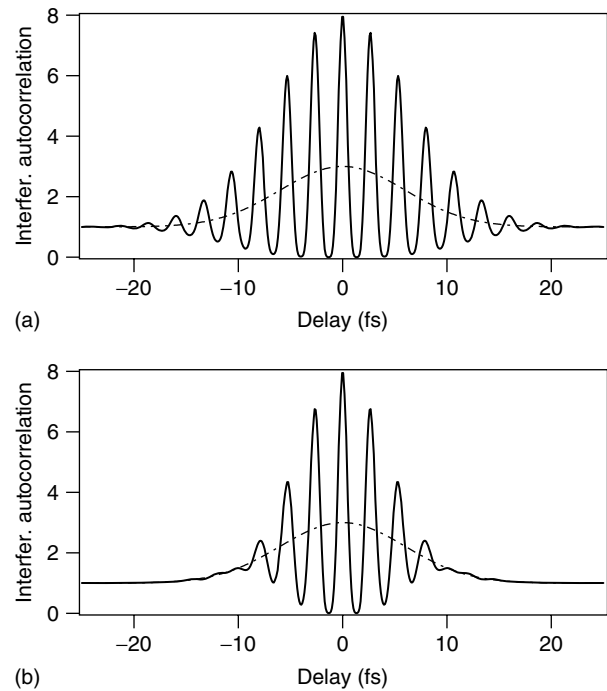


Figure 14 Calculated interferometric autocorrelations of two 10-fs Gaussian pulses (solid line) (a). Both pulses are identical in pulse shape, which makes them indistinguishable for intensity autocorrelation (dash-dotted curve). The IAC, however, clearly indicates that the pulse in the bottom graph (b) is chirped (linearly chirped in this case). The primary indication for a pulse carrying a chirp in an IAC is that its wings start to lift above the constant background.

recombination are the same for both beams and do not need to be taken into account. The spectrometer thus measures

$$I_{\text{SI}}(\omega) = |E_1(\omega) + E_2(\omega)|^2 = |E_1(\omega)|^2 + |E_2(\omega)|^2 + 2|E_1(\omega)E_2(\omega)| \cos(\varphi_1(\omega) - \varphi_2(\omega)) \quad (15)$$

Only the relative phase between the two interferometer-arms appears in the interference term. If one is interested in the phase of one specific arm, the phase in the other arm needs to be known. The interferometer arm with the known phase is then referred to as the *reference arm*. For most experiments, one is only interested in the second and higher order dispersion contributions to the spectral phase. The knowledge of the reference phase can then be obtained either by keeping the amount of dispersion in the reference arm at a negligible level or by measuring the phase with a self-referencing measurement technique (*see e.g.*, (Fittinghoff *et al.* 1996)).

The maximum relative phase variation that can be measured with spectral interferometry is limited by the spectral resolution of the spectrometer. The phase variation has to be slow enough in order to assure correct sampling of the interferogram in accordance with the Nyquist sampling

theorem. The interferogram is correctly sampled if the period of the cosine function in equation (15) is at least twice the spectral resolution. In practice, a higher than the critical Nyquist sampling rate is desired for a reduced sensitivity to experimental noise and other distortions. A detailed analysis of the limitations of spectral interferometry is given in references (Dorrer 1999, Dorrer *et al.* 2000a, 2000b). Note that most of these limitations do not apply in the case of the SPIDER technique introduced below or are at least of less importance.

There are various methods for the extraction of the phase information from a spectral interferogram. In the following, we will describe one of the most robust techniques for phase extraction, which is based on Fourier analysis.

In practice, one introduces a relative delay τ between the laser pulses propagating along the two interferometer-arms. The corresponding interferogram can then be written as

$$I_{SI}(\omega) = |E_1(\omega)|^2 + |E_2(\omega)|^2 + 2|E_1(\omega)E_2(\omega)| \cos(\Delta\varphi(\omega) + \omega\tau) \quad (16)$$

where $\Delta\varphi(\omega)$ is the phase difference between the two interferometer-arms without the linear contribution from the delay τ . The reason for the introduction of this linear phase becomes clear in the discussion of the inversion algorithm. An example of such a spectral interferogram is shown in Figure 15. It can be clearly seen that all deviations from a linear phase result in a shift of the interference fringes with respect to the purely linear case.

Equation (16) can be further rewritten by replacing the cosine with its complex representation and by making the substitutions $a(\omega) := |E_1(\omega)|^2 + |E_2(\omega)|^2$, $b(\omega) := 2|E_1(\omega)E_2(\omega)|$, and $c(\omega) := \frac{1}{2}b(\omega)\exp(i\Delta\varphi(\omega))$. One then finds for the interferogram

$$I_{SI}(\omega) = a(\omega) + c(\omega)\exp(i\omega\tau) + c^*(\omega)\exp(-i\omega\tau) \quad (17)$$

The asterisk denotes complex conjugation. We now apply a Fourier transform to this data and thus obtain an expression of the form

$$FT\{I_{SI}(\omega)\} = a(t) + c(t - \tau) + c^*(t + \tau) \quad (18)$$

where $a(t)$ and $c(t)$ are the Fourier transforms of the respective frequency-dependent functions. As an example, the magnitude of the Fourier transform of the spectral interferogram plotted as a dashed curve in Figure 15(a) is displayed in Figure 15(b). Equation (18) clearly indicates that the Fourier transform of a spectral interferogram corresponds to a peak around zero time and two side-peaks located at $\pm\tau$. One of these side-peaks is now extracted

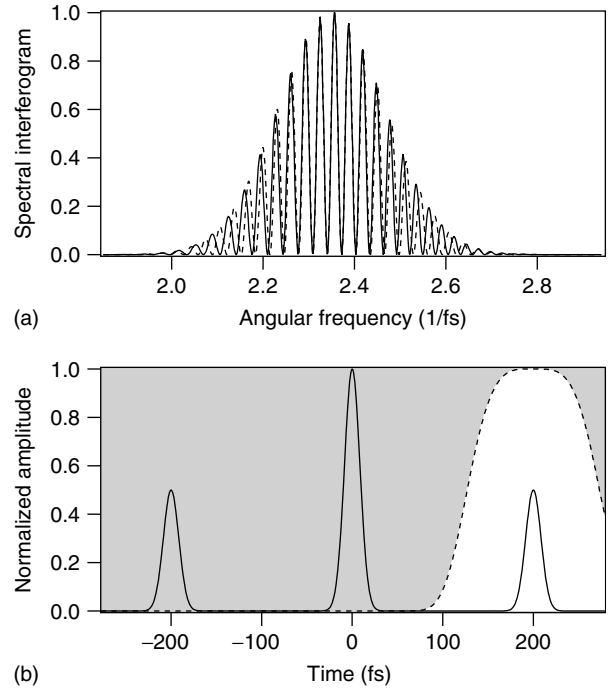


Figure 15 Example of spectral interferogram and its Fourier transform. (a) A spectrum corresponding to a 10-fs transform-limited Gaussian pulse was assumed as the input spectrum of the interferometer. The delay was set to 200 fs. The solid curve results when 3 mm of fused silica glass is present in one of the interferometer arms. The dashed curve is obtained for the same delay but without glass. The difference between the two traces clearly shows the influence of the higher order phase contributions from the piece of fused silica. (b) Fourier transform of dashed interferogram from (a). The dashed curve in (b) represents the filter function used to extract the peak at positive delays.

from the data by multiplying the Fourier transformed data by an appropriate filter function. Without loss of generality we will discuss the case in which the side-peak at positive times is isolated. This peak is represented by $c(t - \tau)$ in equation (18). An inverse Fourier transform of this isolated peak back to the frequency domain thus yields the term $c(\omega)\exp(i\omega\tau)$ from equation (17). Using the definition of $c(\omega)$ and the fact that $b(\omega)$ is a real-valued function, one obtains the desired quantity

$$\Delta\varphi(\omega) = \arg(c(\omega)) = \arg(c(\omega)\exp(i\omega\tau)) - \omega\tau \quad (19)$$

The most important feature of this last relation is that with this algorithm obviously only the phase information of the interferogram is used. This property renders this inversion procedure immune toward spectral amplitude distortions that are slowly varying with frequency such as frequency-dependent detection efficiency. Only spectral distortions that overlap in the time domain with the side-peaks affect the phase reconstruction. This algorithm still works fine even at a reduced fringe visibility. Moreover,

noise-contributions located outside the temporal range of the side-peak are efficiently removed by application of the filter-function to the time-domain data.

From the discussion of this phase extraction algorithm the role of the delay τ becomes clear. It has to be chosen in such a way that the three peaks obtained by Fourier-transforming the spectral interferogram will be well separated in the time domain. This gives a lower limit on τ . The upper limit is determined by the spectral resolution of the spectrometer. It may be noted that the above algorithm does not only work for frequency and time but for any pair of conjugate quantities. Therefore, it is for example possible to extract phase as a function of wavelength by Fourier-transforming an interferogram recorded on an equidistant wavelength scale into its conjugate domain and back again.

3.1.3 FROG

FROG measures the spectrally resolved signal generated in an autocorrelation-like experiment. This autocorrelation involves the interaction of two or three pulse replicas in a second-order or third-order nonlinear medium with instantaneous response. The different implementations of FROG are referred to as *FROG geometries*. Here, we limit the discussion to the most common geometry called *second harmonic generation FROG* (SHG-FROG). SHG-FROG can be considered as a spectrally resolved intensity autocorrelation. Its setup is obtained by replacing the detector in Figure 12(a) with a spectrometer. A detailed discussion of FROG including the other geometries is given in the book by Trebino (2002).

The two-dimensional data set recorded by an SHG-FROG setup is described by

$$S_{\text{FROG}}^{\text{SHG}}(\omega, \tau) = \left| \int_{-\infty}^{\infty} E(t)E(t - \tau) \exp(i\omega t) dt \right|^2 \quad (20)$$

An example of an SHG-FROG trace is shown in Figure 16. Not surprisingly, SHG-FROG possesses the same time-reversal symmetry as the intensity autocorrelation. In other words, the pulse $E(t)$ and its time-reversed replica $E(-t)$ yield the same SHG-FROG trace and are therefore indistinguishable for pulse reconstruction. In practice, this ambiguity can easily be resolved in one of the several ways. One way is to make a second FROG measurement after placing a piece of glass in the beam path. Only one of the two possible pulses is consistent with both measurements. Another way is to know something about the pulse in advance, such as the sign of its chirp. And finally, placing a thin etalon in the beam before the beamsplitter produces a small trailing satellite pulse. If this satellite precedes the reconstructed pulse, the algorithm obviously converges to

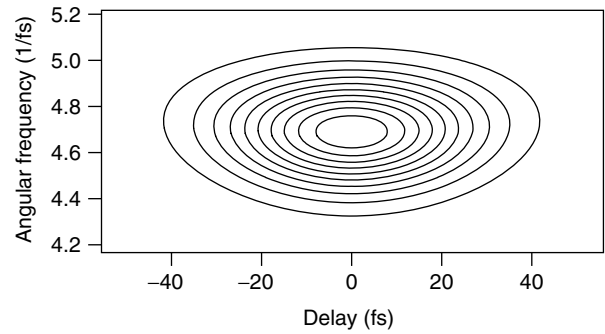


Figure 16 SHG-FROG trace of an initially transform-limited 10-fs Gaussian pulse after propagation through 3 mm of fused silica glass. The contours are evenly spaced on a linear scale.

the time-reversed version of the input pulse. Another ambiguity in SHG-FROG appears if the input pulse consists of two or more well separated sub-pulses. In this case, relative phases of φ and $\varphi + \pi$ between the individual sub-pulses yield the same FROG trace and hence cannot be distinguished. In most practical cases, however, this ambiguity will not pose a severe limitation.

A wide variety of algorithms have been proposed for the iterative retrieval of a pulse from its FROG trace. Conventionally, these algorithms use the following error metric as a measure for convergence:

$$G = \sqrt{\frac{1}{N^2} \sum_{i,j=1}^N |I_{\text{FROG}}(\omega_i, \tau_j) - \alpha I_{\text{FROG}}^{\text{meas}}(\omega_i, \tau_j)|^2} \quad (21)$$

$I_{\text{FROG}}^{\text{meas}}(\omega, \tau)$ denotes the measured FROG data, $I_{\text{FROG}}(\omega, \tau)$ is the FROG trace calculated from the retrieved or reconstructed pulse, α is a scaling factor, and N is the size of the $(N \times N)$ FROG data matrix. The scaling factor is chosen to minimize G . G is generally referred to as the *FROG error*. For experimental data free of systematic errors and proper convergence of the algorithm, the lowest attainable FROG error depends on the grid size N , the percentage of the grid being covered by actual experimental data, and on the amount of noise present in the measured FROG trace. Pulse reconstruction with FROG is essentially an optimization problem. The algorithm tries to iteratively improve guesses for the pulse electric field $E(t)$ with the goal of minimizing the FROG error G . The guess approximates the original experimental pulse shape arbitrarily well if the algorithm converges to a sufficiently low value of G .

Typically, the FROG trace is sampled on a $N \times N$ grid, with N being a power of two. With this particular choice the fast Fourier-transform algorithm (FFT) can be employed in the pulse reconstruction algorithm. The FROG trace is properly sampled when all the nonzero FROG data lies

within the grid. Because, for analytical pulse shapes, in a strict mathematical sense, the FROG-trace data never goes to zero, a more practical criterion for proper sampling has to be found. Usually, FROG-trace data is considered to be properly sampled if all of the data points with an intensity of greater than $\sim 10^{-4}$ of the peak of the trace lie within the grid.

Although FROG traces sampled according to the above criterion will in principle yield the correct pulse, often an equal sampling in time and frequency is preferred in order to improve the robustness of the pulse retrieval algorithm and keep the grid size reasonably low. For pulses with a bell-shaped spectral and temporal shape, equal sampling can be obtained by setting the delay step size to $\Delta\tau = \tau_p/M$ and the frequency step size to $\Delta f = \Delta\omega/(2\pi M)$, where τ_p and $\Delta\omega$ denote the FWHM of the temporal intensity and spectrum, respectively. On a FROG trace of $N \times N$ pixels, the fast Fourier transform relates the frequency step size to the delay step size by $\Delta f = 1/(N\Delta\tau)$. It follows that equal sampling is achieved with

$$M = \sqrt{\tau_p \frac{\Delta\omega}{2\pi} N} \quad (22)$$

A large variety of different measurement techniques exist that are modifications or extensions of the FROG technique. An exhaustive description of the different members of the FROG family is found in the book by Trebino (2002).

3.1.4 SPIDER

SPIDER is a self-referencing variant of spectral interferometry. As discussed above, conventional spectral interferometry measures the spectral phase differences between two pulses. To access the spectral phase of a single pulse, SPIDER generates a spectral shear between the carrier frequencies of two replicas of this pulse. The phase information of the resulting interferogram allows the direct reconstruction of the spectral phase of the input pulse. The spectral shear is generated by upconversion of the two replicas with a strongly chirped pulse using sum-frequency generation (SFG) in a nonlinear optical crystal (Figure 17). Alternatively, downconversion employing difference-frequency generation (DFG) may be used. Without loss of generality we will restrict our discussion to the upconversion case.

It is convenient but not a necessity to directly derive the chirped pulse from the pulse to be measured. This can be done by propagating a fraction of the input beam through a dispersive element. The upconverter pulse has to be stretched such that its instantaneous frequency can be considered as constant for the duration of the pulse to be measured. Being separated by a delay τ much

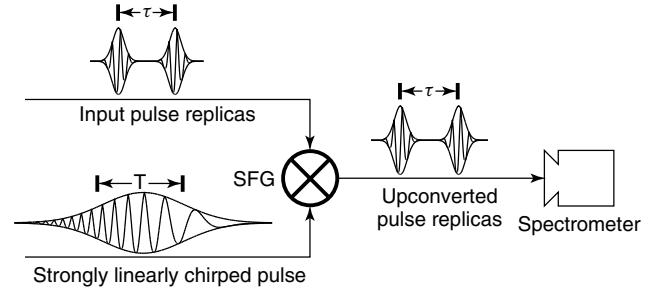


Figure 17 Schematic of the SPIDER technique. Two replicas of the input pulse separated by a delay τ are upconverted with a strongly linearly chirped pulse. The resulting frequency-shifted pulses are brought to interference in a spectrometer.

longer than the pulse duration τ_p , the two replicas are upconverted by different portions of the chirped pulse with different frequencies. The resulting spectral interference pattern $I_{\text{SPIDER}}(\omega)$ of the upconverted short pulse replicas is of the form

$$I_{\text{SPIDER}}(\omega) = |E(\omega)|^2 + |E(\omega + \delta\omega)|^2 + 2|E(\omega)E(\omega + \delta\omega)| \times \cos(\varphi(\omega + \delta\omega) - \varphi(\omega) + \omega\tau) \quad (23)$$

where $\delta\omega$ denotes the spectral shear. This result corresponds to equation (15) with the two frequency-sheared replicas as the interfering pulses. The phase information contained in the cosine term of equation (23) can be extracted by the noniterative, purely algebraic method described in Section 3.1.2.

The constant delay τ is determined once by spectral interferometry of the two short pulse replicas. After subtraction of the linear phase term $\omega\tau$, one obtains the spectral phase $\varphi(\omega)$ at evenly spaced frequencies $\omega_i = \omega_0 + i\delta\omega$ by adding up the appropriate phase differences $\Delta\varphi(\omega_i) = \varphi(\omega_i + \delta\omega) - \varphi(\omega_i)$ according to the following procedure:

$$\Delta\varphi(\omega_i) = \varphi(\omega_i + \delta\omega) - \varphi(\omega_i) = \varphi(\omega_{i+1}) - \varphi(\omega_i) \quad (24)$$

This relation is easily rewritten as

$$\varphi(\omega_{i+1}) = \varphi(\omega_i) + \Delta\varphi(\omega_i) \quad (25)$$

By continuing the recursion, one obtains

$$\begin{aligned} \varphi(\omega_{i+1}) &= \varphi(\omega_{i-1}) + \Delta\varphi(\omega_{i-1}) + \Delta\varphi(\omega_i) \\ &= \varphi(\omega_1) + \Delta\varphi(\omega_1) + \dots + \Delta\varphi(\omega_i) \end{aligned} \quad (26)$$

The phase constant $\varphi(\omega_1)$ remains undetermined but is only a constant offset of the entire reconstructed spectral phase $\varphi(\omega)$, which does not affect the temporal pulse shape. Thus,

one may set $\varphi(\omega_1) = 0$. This yields a compact relation for the spectral phase of the input pulse

$$\varphi(\omega_{i+1}) = \sum_{n=1}^i \Delta\varphi(\omega_n) \quad (27)$$

If the shear is small relative to the variation of the spectral phase, the phase differences may be approximated by the first derivative of the spectral phase. In this case, the spectral phase can be obtained by integration

$$\varphi(\omega) \approx \frac{1}{\delta\omega} \int \Delta\varphi(\omega) d\omega \quad (28)$$

In the final step of pulse reconstruction, the complex frequency-domain representation of the electric field of the pulse $E(\omega) \propto \sqrt{I(\omega)}e^{i\varphi(\omega)}$ is obtained from the retrieved spectral phase and an independent measurement of the power spectrum $I(\omega)$. Fourier transforming these results yields the temporal pulse shape.

Inaccuracies in the determination of the linear phase term $\omega\tau$ associated with the delay τ show up as errors in the reconstructed phase. Such inaccuracies can be caused by differences between the wavelength calibration used for the measurement of the linear phase and the one used for the measurement of the SPIDER interferogram. These problems are suitably avoided if the linear phase is derived from the second harmonic of the two pulse replicas rather than from their fundamental. Because this signal spectrally overlaps with the SPIDER interferogram, this allows using the same calibration for the SPIDER and the linear phase data and cancels out most of the calibration errors in the process of subtracting the linear phase from the SPIDER interferogram phase.

There are three parameters in the design of the SPIDER apparatus. One is the delay τ between the two short pulse replicas, the next is the spectral shear $\delta\omega$, and the final one is the group-delay dispersion GDD_{up} used to generate the strongly linearly chirped upconverter pulse. These three parameters are, however, not independent. The spectral shear is given by

$$\delta\omega = \frac{\tau}{GDD_{\text{up}}} \quad (29)$$

This relation is also used to determine the spectral shear in the experiment. The exact delay τ is obtained from the measurement of the phase term $\omega\tau$ described above. And GDD_{up} is either measured using spectral interferometry or calculated from the known dispersion properties of the pulse stretcher.

The criterion for choosing the delay τ follows the same guidelines as were discussed in the case of spectral interferometry. Typically, 20–30 fringes across the interferogram

were found to work well. One should choose the spectral shear such that the time window $2\pi/\delta\omega$ is at least ten times greater than the transform-limited input pulse duration. For bell-shaped spectra, a ratio between shear and bandwidth of $\delta\omega/\Delta\omega \approx 1/4$ already gives good results. For more box-shaped spectra or more complex pulses, this ratio has to be reduced and values of $\delta\omega/\Delta\omega$ down to a few percent might be required. Once a delay and a spectral shear have been determined, the required group-delay dispersion GDD_{up} follows from equation (29). Independently from this relation, GDD_{up} has to be chosen large enough in order to ensure that the two short pulse replicas are upconverted with quasi-cw slices of the strongly linearly chirped pulse.

As was the case with FROG, several variations and extensions of the SPIDER technique exist. The spatially encoded arrangement for SPIDER (SEA-SPIDER) and the zero additional phase SPIDER (ZAP-SPIDER) are particularly noteworthy. SEA-SPIDER transfers the interference from the spectral to the spatial domain, which allows to overcome some sampling limitations of conventional SPIDER (Kosik *et al.* 2005). ZAP-SPIDER enables the measurement of ultrashort pulses without introducing any dispersion in the measurement setup (Baum *et al.* 2004). A detailed discussion of SPIDER can be found in the article by Walmsley (2004).

4 HIGH-ORDER HARMONIC GENERATION

With amplified femtosecond laser pulses, the electrical field-strength of the beam can easily reach and surpass inner-atomic field strengths. In this regime, the interaction of the light field with the atoms cannot be considered as a simple perturbation anymore. One process occurring in this nonperturbative regime is high-order harmonic generation (Ferry *et al.* 1988). It can be exploited for the extension of femtosecond pulse sources into the VUV to soft-X-ray spectral region and even for the generation of attosecond pulses. The process of HHG can be described semiclassically with the so-called three-step model (Corkum 1993). It is usually sufficient for the qualitative understanding of many aspects of HHG. We thus limit our discussion to this model. The concept underlying the three-step model is schematically depicted in Figure 18. The strong electric field of the driving laser significantly deforms the Coulomb potential of the atom. In step 1, around a maximum of the laser field, an electron may leave the atom through tunnel ionization. The evolution of the electron after ionization is then treated purely classically with the driving laser field accelerating the electron. Through this acceleration, the electron gains kinetic energy. As the oscillating

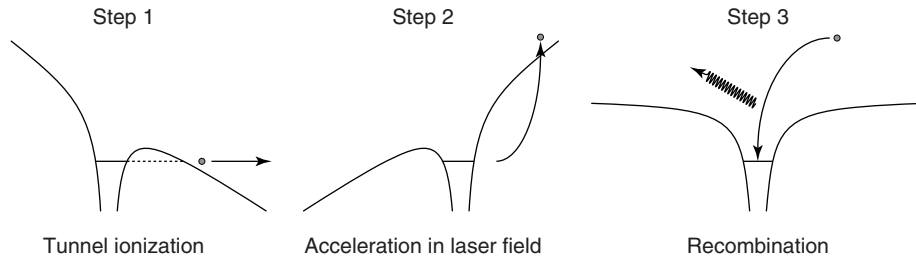


Figure 18 Three-step model of high-order harmonic generation. The three panels show the atomic potential that is deformed by the superimposed laser field. In the first step, the electron is liberated from the atom through tunnel ionization. It is then accelerated in the driving laser field, thereby gaining kinetic energy. In the third step, the electron recombines with the parent ion and emits a photon containing the excess energy.

electric field of the laser changes its sign a quarter period after the maximum, the electron is slowed down and is eventually driven back toward its parent ion. With a certain probability, the electron then recombines with the ion in the third step of the process. Upon recombination, the electron releases the excess energy corresponding to the gained kinetic energy plus the ionization energy of the atom in the form of a photon. This photon can be much more energetic than the driving laser photon.

Owing to the symmetry of the system, the three-step process described above repeats in every half-cycle of the driving laser field. From this periodicity in the emission of the energetic photons, it directly follows that the spectrum of the generated radiation consists of discrete peaks located at odd integer multiples of the laser photon energy. It lies in the nonperturbative nature of HHG that those peaks may extend to very high integer multiples. The peak photon yield of the perturbative harmonics known from classical nonlinear optics (third harmonic, fifth harmonic, and maybe even seventh harmonic) drops exponentially with increasing harmonic order. It is typical for HHG that around the seventh to ninth harmonic, a transition to a plateau of almost constant photon yield takes place. This plateau region can extend over many (even hundreds) harmonic orders before it reaches the cutoff where conversion efficiency drops exponentially towards zero. The location of the cutoff can be estimated using the cutoff law

$$\hbar\omega_{\text{cut-off}} = 3.17U_p + I_p \quad (30)$$

where $\omega_{\text{cut-off}}$ denotes the cutoff angular frequency, I_p the ionization potential of the HHG medium, and U_p the ponderomotive energy. The ponderomotive energy is given by

$$U_p = \frac{e^2 E_0^2}{4m_e \omega^2} \quad (31)$$

Here, e is the electron charge, E_0 the laser electric-field amplitude, and m_e the electron mass. One can see

that the higher the laser intensity, the higher the cutoff. The maximum useful intensity is, however, limited to well below the intensity at which the tunneling barrier is completely suppressed. This and other limiting effects are discussed below. At constant intensity, a longer driving laser wavelength can further extend the cutoff.

When studying the classical trajectories of the electrons in the external electric field of the driving laser pulse, one finds that electrons released between the zero-crossing and maximum amplitude of the field never return to the parent ion. Those electrons do not contribute to HHG. Electrons freed between the field maximum and its next zero crossing, however, return to the parent ion and may recombine. Examples for such classical trajectories are shown in Figure 19. The actual trajectory and the energy gained by the electron depend on its release time. For each energy value below the cutoff, two corresponding trajectories are found: a long trajectory for which the

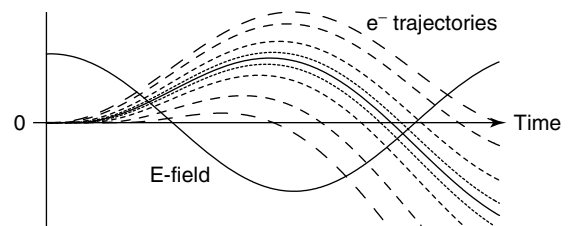


Figure 19 Classical trajectories of electrons (thin lines) released from the atom and accelerated in the electric field of the driving pulse (thick solid line). The trajectory an electron takes depends on the electron release time with respect to the electric field. Recombination with the parent ion can take place at zero-crossings. The kinetic energy at recombination is highest for the cutoff trajectory (thin solid line). The length of the dashes visualizes the recombination energy of the other trajectories: longer dashes represent lower energy. For each energy value below the cutoff, a long and a short trajectory can be found leading to the same recombination energy. The process shown repeats in every half-cycle of the electric field. Electrons released during the first half of the half-cycle (not shown) cannot return to the parent ion and thus do not contribute to HHG.

electron was freed close to the field maximum and a short trajectory with a later electron release time. Figure 19 also clearly illustrates that the harmonic emission from the short family of trajectories possesses an up-chirp in time, while the emission from the long trajectories is down-chirped. These findings obtained from the purely classical picture are in excellent qualitative agreement with quantum mechanical models.

Most commonly, HHG is performed in a gas jet. The three-step model and the rest of the above discussion only take into account how a single atom responds to the strong laser field. However, in a gas jet, the beam interacts with an ensemble of atoms. The high-order harmonic light observed after the generation medium is thus a coherent superposition of the microscopic response of the individual atoms. A significant amount of harmonic light can be observed macroscopically only if the contributions from the individual microscopic emitters add up constructively. For efficient HHG, one therefore needs to ensure phase matching. A review of macroscopic aspects of HHG is given by Gaarde *et al.* (2008). Using waveguides instead of gas jets for HHG and phase matching is reviewed by Paul *et al.* (2006). Phase matching is strongly trajectory dependent. This allows phase matching of only the short trajectory by placing the focus of the driving laser beam in front of the gas jet used for HHG.

The maximum useful laser intensity is limited by the barrier suppression intensity. As soon as the laser intensity gets close to the barrier suppression region, a significant fraction of the atoms in the generation target are ionized and are thus lost for the HHG process. In addition, the plasma dispersion by the created free electrons destroys the phase matching. In the case of short pulses exceeding barrier suppression with their peak intensity, HHG can take place on the not-so-intense leading edge of the pulse, but stops at later times where the intensity rises into the barrier suppression regime. This effect of ionization gating can be exploited as a temporal gate for isolated attosecond pulse generation (*see* Section 4.1).

If HHG is performed for the generation of femtosecond or attosecond pulses in the VUV to soft-X-ray region, typically rare gases are used as the generation medium. With a standard Ti:sapphire amplifier system operating at 800 nm and providing millijoule-level 30-fs pulses, photon energies of several tens of electronvolts can be generated in Ar, while around 100 eV can be reached in Ne. Shorter pulses support even higher photon energies in these gases. Conversion efficiencies in the plateau region of Ar harmonics are usually on the order of 10^{-6} per harmonic and quickly drop above the cutoff. Thus, the energy per plateau harmonic is in the range of a nanojoule in such a typical scenario.

4.1 Attosecond Pulse Generation

Owing to the high nonlinearity of the process, emission from HHG is concentrated to a short fraction of the oscillation cycle of the driving field. With a half-cycle duration of ~ 1.3 fs in the case of pulses from a Ti:sapphire amplifier, it becomes clear that the time signature of harmonic emission is in the subfemtosecond domain. Two operation regimes can be distinguished depending on the duration of the pulse driving the HHG. With long driver pulses, attosecond bursts of harmonic radiation are emitted on every half-cycle of the pulse. The result is a train of attosecond pulses with a femtosecond envelope that is usually somewhat shorter than the initial driver pulse. If few-cycle pulses are used, a single attosecond burst of radiation can be isolated. We further discuss these two regimes below.

4.1.1 Attosecond Pulse Trains

Although attosecond pulse trains (APTs) probably have been created since the early days of HHG (Antoine *et al.* 1996), the first measurement of the attosecond temporal structure was only possible in 2001 (Paul *et al.* 2001). The method used for this measurement is described in Section 4.2.1. For the production of APTs, one usually chooses to phase match the short-trajectory emission from HHG. The individual attosecond pulses within the APT will then carry an up-chirp as briefly mentioned above and illustrated in Figure 19. This chirp can be compensated for by passing the APT through a suitable length of material with negative dispersion. Most materials in the VUV to soft-X-ray spectral region provide negative dispersion. Because thin metal filters are always present in a HHG setup to filter out the strong fundamental and low-order harmonic light, usually appropriately thick metal filters are chosen for pulse compression. Through the choice of filters, generation medium, and driving laser intensity, the center frequency of APTs is tunable to virtually any spectral region that can be covered by HHG. The minimum duration of an individual attosecond pulse in the APT is limited through the available bandwidth, i.e., essentially the number of harmonic lines transmitted through the filter. When generated in argon and after passage through an appropriately chosen aluminum filter for dispersion compensation, durations of individual pulses of well below 200 as have been demonstrated. The envelope of the APT has a duration somewhat shorter than the initial driving pulse. Owing to the underlying periodicity of the HHG process, the individual attosecond pulses are spaced by one half-cycle of the driver wavelength. By adding small amounts of second harmonic light to the driving laser field, the symmetry of the process can be broken, leading to the

generation of odd and even harmonics and a full cycle periodicity of the APT. While isolated attosecond pulses are usually more desirable for straightforward attosecond pump-probe schemes, the periodic structure of APTs can also be exploited in other measurement scenarios. For example, the effect of different pulse sequences in multiple excitation schemes can be investigated by shaping the driving laser field to gain control over the number of pulses in an APT.

4.1.2 *Isolated Attosecond Pulses*

Isolated attosecond pulses have been demonstrated for the first time in 2001. The shortest pulses to date have a duration below 100 as and are centered at photon energy of 80 eV (Goulielmakis *et al.* 2008). The pulse energy contained in these pulses was reported to amount to 0.5 nJ. The key to the generation of an isolated attosecond pulse is to limit high-order harmonic emission to a single half-cycle of the driving infrared laser field. Several methods to achieve this goal have been proposed theoretically. We limit our discussion to the two experimentally demonstrated techniques.

The first successfully implemented method exploited the rapid variation of the electric-field amplitude in a few-cycle laser pulse. In such a short pulse, the peak electric-field amplitude changes considerably from one half-cycle to the next. As a result, the maximum acceleration experienced by the liberated electrons depends strongly on the instance at which they were created by the infrared laser pulse. The maximum kinetic energies are thus only reached by the electrons that have been freed during the half-cycle immediately preceding the half-cycle of highest amplitude within the pulse. This is a direct consequence of the three-step process of HHG. It immediately follows that the highest photon energies produced in the process originate from the electrons liberated during a single half-cycle. The other half-cycles can only contribute to the harmonic emission at lower photon energies. By applying a spectral high-pass filter to the generated radiation, it is therefore possible to extract the photons from a single burst of radiation initiated during a single half-cycle of the driving laser pulse. The spectral signature of such an isolated attosecond burst is a continuum. Through CEP control of the infrared few-cycle pulse, one can maximize the difference in peak amplitude between the strongest and second strongest half-cycle. This is achieved when the peak amplitude of the strongest half-cycle coincides with the peak of the pulse envelope. Such a pulse is commonly referred to as *cosine pulse*. Because the largest continuum bandwidth is obtained with a cosine pulse, this is usually the preferred mode of operation for isolated attosecond pulse production. The other extreme is represented by the sine

pulse (i.e., CEP shifted by 90° with respect to a cosine pulse). In this case, the maximum field strength is reached during two consecutive half-cycles of the pulse and, thus, two bursts of harmonic emission are found at the highest photon energies.

Another method to limit harmonic emission to a single half-cycle makes use of the strong polarization dependence of HHG. When considering the three-step model in three-dimensional space, it becomes clear that only linear polarization can reliably drive the electron back to its parent ion. The electron will in general miss the ion for elliptical or circular polarization. In this case, recombination cannot take place and HHG is effectively suppressed. HHG is restricted to a short time window by preparing the polarization state of the driving few-cycles pulse such that it is elliptical most of the time and linear only within a brief time window. This particular polarization state can be obtained by passing the pulses through an arrangement of a multiorder and a zero-order quarter wave plate. This technique is commonly referred to as *polarization gating*. The shortest pulses generated so far with this method have a duration of 130 as at 36-eV photon energy (Sansone *et al.* 2006).

Isolated attosecond pulses are attractive because of their straightforward use in pump-probe schemes. So far, one of the two pulses is a few-cycle infrared pulse due to the small cross sections for two-photon processes in the VUV to soft-X-rays. True pump-probe measurements using two attosecond pulses might become feasible in the future with more efficient attosecond pulse generation schemes. The two-color pump-probe schemes employing an infrared and an attosecond pulse are closely related to the basic ideas underlying the attosecond pulse characterization methods described in detail below. See (Corkum and Krausz 2007) for a review of recent attosecond time-resolved experiments. The time resolution is limited by the attosecond pulse duration. It may be noted that attosecond time resolution can also be achieved by methods that do not require attosecond pulses. An example is attosecond angular streaking, which measures the angularly resolved momentum distribution of electrons and ions created by strong-field ionization with near-circularly polarized few-cycles laser pulses (Eckle *et al.* 2008b). Temporal resolution is obtained by mapping angle to time with 360° corresponding to one laser cycle. This method was successfully applied to measure an upper bound to tunneling time in field ionization of helium (Eckle *et al.* 2008a).

4.2 Attosecond Pulse Characterization

Two methods for amplitude and phase characterization of attosecond pulses have been demonstrated experimentally (Muller 2002, Mairesse and Quéré 2005). Both techniques

exploit the nonlinear interaction of an infrared field with the attosecond burst. This is due to the small cross sections for two-photon processes in the VUV to soft-X-ray spectral region, which often prevents the use of autocorrelation techniques analogous to those known from femtosecond pulse diagnostics in the infrared spectral region. This fundamental experimental difficulty exists for any time-resolved measurement with high-photon-energy sources based on HHG. The two-color approach used in attosecond pulse diagnostics is therefore also representative for most attosecond time-resolved experiments performed so far.

Furthermore, both attosecond pulse characterization methods share in common that they do not directly measure the attosecond light pulse but rather an electron wave packet generated by this pulse and interacting with the infrared light field. The attosecond electron wave packets are created by linear absorption of the attosecond light pulse in a target gas and its resulting ionization. Both methods, therefore, assume a certain mapping of the attosecond light pulse structure onto the measured electron wave packet structure. This issue is discussed below together with further details specific to each individual characterization method.

4.2.1 RABBITT

Reconstruction of attosecond harmonic beating by interference of two-photon transitions (RABBITT, (Muller 2002, Paul *et al.* 2001)) is a measurement technique that is specialized on the characterization of APTs. It is closely related to the SPIDER technique used for femtosecond pulses in the visible to near-infrared spectral domain. In its most common implementation, it measures the average shape of the attosecond pulses within the pulse train, neglecting pulse-to-pulse variations. In the experimental setup, a collinear superposition of the fundamental laser beam and the APT generated by this laser is focused into a target gas (typically argon). The relative delay between the infrared beam and the APT can be adjusted. The process taking place in the target gas is schematically depicted in Figure 20. The individual harmonics forming the APT get absorbed in the target and produce free electrons through ionization. These electrons are detected by a time-of-flight electron spectrometer. The harmonic spectrum of the APT directly maps onto the electron spectrum because the electron energy distribution is given by $E_{\text{kin}} = q_i \hbar \omega_0 - I_p$, with q_i representing the harmonic order, ω_0 the fundamental laser angular frequency, and I_p the ionization potential of the target gas. Because the APT consists only of odd-order harmonics, the corresponding peaks in the electron spectrum are separated in energy by $2\hbar\omega_0$. In the presence of an additional laser field at the fundamental laser frequency, an infrared photon can be absorbed or emitted in the absorption process. This leads to the creation of sidebands located between

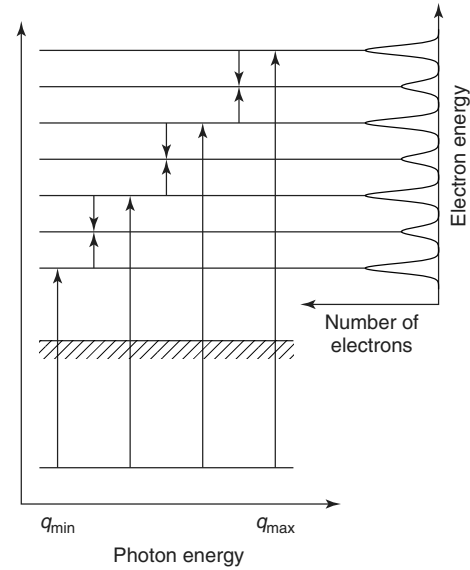


Figure 20 Basic phase detection principle underlying RABBITT. The individual harmonics forming the APT are absorbed in the target gas. Sidebands in the electron spectra are created through interaction with the additional infrared field. At sufficiently low infrared intensity, only the two neighboring harmonics significantly contribute to a given sideband. The contributions from these two harmonics interfere. The relative phase of two neighboring harmonics can be extracted by scanning the delay and monitoring the amplitude modulations in the sideband. The chirp of the individual attosecond pulses is obtained from the measured phase shifts between the modulations seen on the various sidebands.

the peaks resulting from the odd harmonics. It can be assured with sufficiently low infrared intensity that only one infrared photon is exchanged and thus only neighboring peaks contribute significantly to a given sideband. Different phases in the harmonics that form the APT map to different phases in the corresponding peaks in the electron spectrum. The differing phases of two neighboring peaks thus lead to interference in the common sideband. When identifying the different phase contributions, the electron count in a sideband is found to follow

$$I_{q+1} \propto \cos\left(2\omega_0\tau + \varphi_q - \varphi_{q+2} + \Delta\varphi_{q+1}^{\text{atomic}}\right) \quad (32)$$

where φ_q and φ_{q+2} represent the phase values of two neighboring harmonics with q denoting the order of the lower of the two harmonics. The delay between the infrared field and the APT is described by τ . $\Delta\varphi_{q+1}^{\text{atomic}}$ is an intrinsic phase added in the two-photon process through the complex transition matrix elements. It is usually small compared to the other terms and can be obtained from theory with high accuracy.

Experimentally, the sideband electron count is recorded as a function of delay τ . Fitting a cosine to the modulated electron yield allows extracting the phase difference

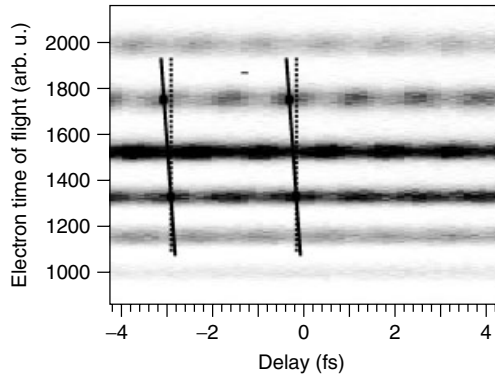


Figure 21 Experimental RABBITT trace. The figure shows the recorded electron spectrum as a function of delay between the infrared pulse and the APT. The dots mark the location of local electron count maxima in the sidebands. The solid lines connecting each pair of dots illustrate the phase shift between the sidebands. In the absence of phase shifts, the dots would be located on the dashed lines.

$\varphi_q - \varphi_{q+2}$ for each sideband. In practice, Fourier transform based methods are used for phase extraction with better accuracy. The phase across the harmonics forming the APT can now be determined in analogy to the algorithm introduced for the SPIDER pulse characterization method. Following the procedure described by equation (26) we obtain the spectral phase of the APT. A Fourier transform together with the recorded harmonic spectrum then yields the attosecond pulse shape. It may be noted that RABBITT determines only one average phase value per harmonic line. In reality, the spectral phase is not constant over a harmonic peak. Because of this missing information, pulse-to-pulse variations within the train cannot be characterized by RABBITT and no information about the shape of the envelope of the APT can be retrieved. The reconstructed shape represents the average attosecond pulse shape for all pulses within an infinitely extended pulse train.

Figure 21 shows an experimental RABBITT data set recorded in our laboratory. The periodic modulation of the sidebands as a function of delay between the infrared pulse and the APT can be clearly seen. Modulations in anti-phase to the sideband signal appear on the peaks created by direct single-photon absorption of the APT harmonics. This is because the infrared field transfers the sideband electrons from the single-photon absorption peaks to the sidebands, thereby reducing the electron count on the main peaks. The phase shift observed between the sidebands indicates the presence of a chirp in the measured APT.

4.2.2 FROG CRAB

Characterization of the temporal profile of isolated attosecond pulses is commonly done with frequency-resolved optical gating for complete reconstruction of attosecond bursts

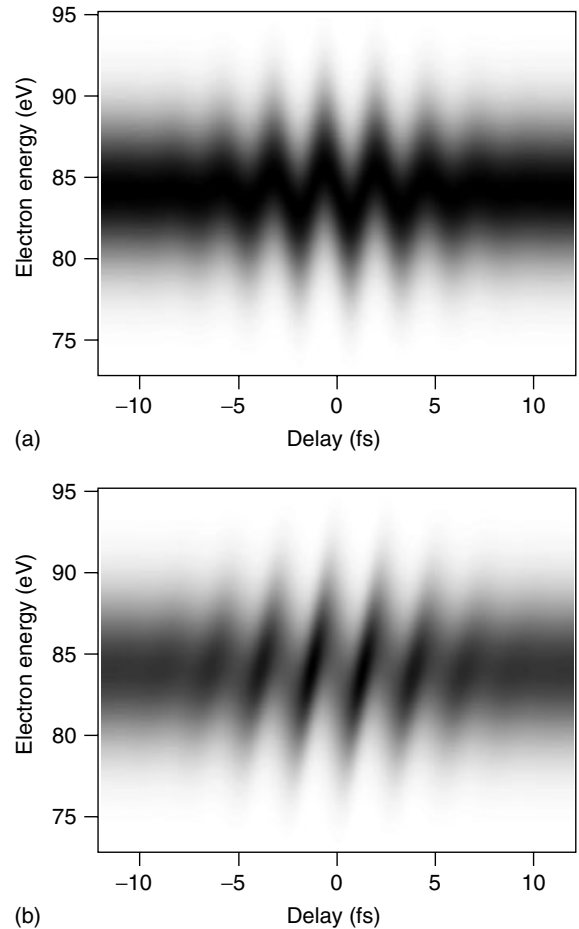


Figure 22 Calculated FROG CRAB traces. The infrared pulse is an unchirped Gaussian 6-fs pulse centered at 800-nm wavelength and with a peak intensity of $5 \times 10^{10} \text{ W cm}^{-2}$ for both cases. The attosecond pulse is centered at 100 eV, the detection medium is argon, and the detection direction is along the laser polarization. In (a), an unchirped 250-as pulse has been used as the input, while a positively chirped attosecond pulse with the same 250-as transform limit served as the input in (b).

(FROG CRAB, (Mairesse and Quéré 2005)). The experimental setup required for FROG CRAB is identical to the one used for RABBITT. Again, the attosecond pulse and an infrared field are collinearly focused into a detection medium. As it was the case for RABBITT, FROG CRAB is based on the photo-ionization of the target gas by the attosecond pulse in the presence of an infrared laser field. In the classical picture, the low-frequency laser field accelerates the continuum electrons created by the attosecond pulse. This leads to a modulation of the electron kinetic energy that depends on the instance of ionization with respect to the infrared pulse and thus on the time delay between the two pulses. Figure 22 shows calculated examples for FROG CRAB traces.

When doing a more accurate treatment of the physical process underlying FROG CRAB, one finds that the

transition amplitude to the final continuum state $|\nu\rangle$ with momentum ν is given by

$$a(\nu, \tau) = -i \int_{-\infty}^{+\infty} dt e^{i\phi(t)} \mathbf{d}_{p(t)} \times \mathbf{E}_{\text{AP}}(t - \tau) e^{i(W + I_p)t} \quad (33)$$

$$\phi(t) = - \int_t^{+\infty} dt' (\nu \cdot \mathbf{A}(t') + \mathbf{A}^2(t')/2) \quad (34)$$

with $\mathbf{d}_{p(t)}$ the dipole transition matrix element, $\mathbf{E}_{\text{AP}}(t)$ the electric field of the attosecond pulse, $W = \nu^2/2$ the kinetic energy of the electron, and $\mathbf{A}(t)$ the vector potential of the infrared pulse (Mairesse and Quéré 2005). These equations hold in the strong field approximation and are given in atomic units for consistency with the literature. It can be seen from the above expressions that the infrared pulse essentially acts as a phase modulator for the electron wavepacket $\mathbf{d}_{p(t)} \mathbf{E}_{\text{AP}}(t)$. Furthermore, the electron spectrum as a function of delay as obtained from equation (33) closely resembles a more generalized version of equation (20) known from the SHG FROG pulse characterization method. In fact, a general FROG trace can be written as

$$S(\omega, \tau) = \left| \int_{-\infty}^{+\infty} dt G(t) E(t - \tau) e^{i\omega t} \right|^2 \quad (35)$$

with $E(t)$ representing the pulse to be characterized and $G(t)$ a so-called gate function, which is given by $E(t)$ in the case of SHG FROG.

Blind FROG is a method known from femtosecond pulse diagnostics that allows reconstructing an unknown gate function $G(t)$ and an unknown pulse $E(t)$ simultaneously from a single data set of the form defined by equation (35) (Trebino 2002). The price that has to be paid compared to conventional FROG for not knowing the gate function is a reduced robustness of the algorithm and the potential occurrence of nontrivial ambiguities. The basic idea behind pulse reconstruction with Blind FROG is the same as that for any other incarnation of FROG. The algorithm iteratively improves guesses for the gate function and the pulse seeking to minimize the mean square deviation between the measured and the reconstructed FROG trace. Because the electron spectrum in a FROG CRAB measurement is according to equation (33) of the form described by equation (35), we can use the Blind FROG approach to retrieve the attosecond pulse $E_{\text{AP}}(t)$ and the phase gate induced by the infrared pulse. The electric field of the infrared pulse can be obtained from the reconstructed phase gate and can be verified with independent femtosecond diagnostics for consistency. We have therefore simultaneously characterized the attosecond and the infrared pulse.

So far FROG CRAB was mainly applied to the measurement of isolated attosecond pulses, but can also be used for the reconstruction of APTs. FROG CRAB is capable of retrieving the exact shape of the APT including pulse shape variations within the train and the shape of the envelope. For a successful application of the algorithm, however, high fidelity data is needed. In particular, the energy resolution of the electron spectrometer needs to be sufficiently high. The required energy resolution is inversely proportional to the infrared pulse duration used for the APT generation (i.e., on the order of 0.1 eV for a 30-fs driver pulse).

5 OUTLOOK TOWARDS HIGHER PHOTON ENERGIES

In this article, we have focused our discussion on the most common sources of femtosecond and attosecond pulses. Already these sources cover photon energies from well below 1 eV to hundreds of electronvolts. With the extension of HHG to longer driver wavelengths, tabletop attosecond sources approaching the kiloelectronvolts range might become available. Less compact setups hold promise for the extension of femtosecond and attosecond pulses toward even higher photon energies. Relativistic laser-matter interaction is predicted to yield attosecond bursts with kiloelectronvolts photon energy in various configurations. In one scheme, a few-cycle infrared laser pulse is focused at a relativistic intensity onto a solid target under vacuum (Tsakiris *et al.* 2006). At the vacuum-solid interface, the laser produces an oscillating plasma interacting with the laser field. This back-action gives rise to the generation of harmonic radiation in the beam reflected at the target. Under proper operating conditions, spectral filtering of the harmonic radiation yields an isolated attosecond pulse.

Future free-electron laser facilities are expected to produce energetic attosecond pulses in the X-ray (Zholents and Fawley 2004, Saldin *et al.* 2002). In free-electron lasers, a dense bunch of electrons from a linear accelerator is injected into an undulator. The undulator periodically deflects the electrons with static magnetic fields. With the undulator period properly tuned for the desired emission wavelength of the laser, the bremsstrahlung from one wiggling electron may interfere constructively with its radiation emitted further down-stream of the undulator. However, with low electron densities, the radiation contributions from an ensemble of electrons still add up incoherently. In case of sufficiently high electron density, the generated radiation acts back on the electron bunch. Owing to this back-action, the electron bunch may form

a periodic structure of micro-bunches, which enables the coherent addition of the radiation generated within the electron ensemble. In the most common schemes, laser action starts from self-amplified spontaneous emission. This leads to an inherently stochastic characteristic of such sources and large pulse-to-pulse fluctuations are to be expected. Seeding the free electron-laser may reduce this problem.

The relativistic high-order harmonics sources and the free-electron lasers still undergo a rapid development. Considerable improvements of their characteristics and many exciting applications of these sources can be expected during years to come.

ABBREVIATIONS AND ACRONYMS

APT	attosecond pulse trains
BBO	beta barium borate
CEP	carrier-envelope offset phase
CPA	chirped-pulse amplification
DFG	difference-frequency generation
FFT	fast Fourier-transform
FROG CRAB	frequency-resolved optical gating for complete reconstruction of attosecond bursts
FROG	frequency-resolved optical gating
FWHM	full width at half maximum
GDD	group delay dispersion
HHG	high-order harmonic generation
IAC	interferometric autocorrelation
KLM	Kerr-lens modelocking
NOPA	noncollinear OPA
OPA	optical parametric amplifier
OPCPA	optical parametric chirped-pulse amplifier
OPG	optical parametric generation
RABBITT	reconstruction of attosecond harmonic beating by interference of two-photon transitions
SAM	self-amplitude modulation
SEA-SPIDER	spatially encoded arrangement for SPIDER
SESAM	semiconductor saturable absorber mirror
SFG	sum-frequency generation
SHG-FROG	second harmonic generation FROG
SHG	second harmonic generation
SPIDER	spectral phase interferometry for direct electric-field reconstruction
SPM	self-phase modulation
TOD	third-order dispersion
VUV	vacuum ultraviolet
XUV	extreme ultraviolet
ZAP-SPIDER	zero additional phase SPIDER

REFERENCES

- Agrawal, G.P. (2001) *Nonlinear Fiber Optics*, Academic Press, San Diego, CA.
- Antoine, P., L'huillier, A., and Lewenstein, M. (1996) Attosecond pulse trains using high-order harmonics. *Physical Review Letters*, **77**, 1234–1237.
- Aus der Au, J., Kopf, D., Morier-Genoud, F., Moser, M., and Keller, U. (1997) 60-fs pulses from a diode-pumped Nd:glass laser. *Optics Letters*, **22**, 307–309.
- Baltuska, A., Fuji, T., and Kobayashi, T. (2002) Controlling the carrier-envelope phase of ultrashort light pulses with optical parametric amplifiers. *Physical Review Letters*, **88**, 133901.
- Baltuska, A., Udem, T., Uiberacker, M., Hentschel, M., Goulielmakis, E., Gohle, C., Holzwarth, R., Yakovlev, V.S., Scrinzi, A., Hänsch, T.W., *et al.* (2003) Attosecond control of electronic processes by intense light fields. *Nature*, **421**, 611–615.
- Baum, P., Lochbrunner, S., and Riedle, E. (2004) Zero-additional-phase SPIDER: full characterization of visible and sub-20-fs ultraviolet pulses. *Optics Letters*, **29**, 210–212.
- Bosenberg, W.R. and Eckhardt, R.C. (1995) Optical parametric devices, special feature issue. *Journal of the Optical Society of America*, **12**, 2005–2322.
- Brunner, F., Innerhofer, E., Marchese, S.V., Südmeyer, T., Paschotta, R., Usami, T., Ito, H., Kurimura, S., Kitamura, K., Arisholm, G., *et al.* (2004) Powerful red-green-blue laser source pumped with a mode-locked thin disk laser. *Optics Letters*, **29**, 1921–1923.
- Brunner, F., Südmeyer, T., Innerhofer, E., Paschotta, R., Morier-Genoud, F., Gao, J., Contag, K., Giesen, A., Kisel, V.E., Shcherbitsky, V.G., *et al.* (2002) 240-fs pulses with 22-W average power from a mode-locked thin-disk Yb:KY(WO₄)₂ laser. *Optics Letters*, **27**, 1162–1164.
- Byer, R.L. and Piskarskas, A. (1993) Optical parametric oscillation and amplification, special feature issue. *Journal of the Optical Society of America*, **10**, 1977–2243.
- Cerullo, G. and Silvestri, S.D. (2003) Ultrafast optical parametric amplifiers. *Reviews of Scientific Instruments*, **74**, 1–17.
- Corkum, P.B. (1993) Plasma perspective on strong-field multiphoton ionization. *Physical Review Letters*, **71**, 1994–1997.
- Corkum, P.B. and Krausz, F. (2007) Attosecond science. *Nature Physics*, **3**, 381–387.
- Diels, J.-C., Stryland, E.W.V., and Gold, D. (1978) Investigation of the parameters affecting subpicosecond pulse durations in passively mode locked dye lasers. *First International Conference on Picosecond Phenomena*, Hilton Head, South Carolina, USA.
- Dorrer, C. (1999) Influence of the calibration of the detector on spectral interferometry. *Journal of the Optical Society of America*, **16**, 1160–1168.
- Dorrer, C., Belabas, N., Likforman, J.-P., and Joffre, M. (2000a) Experimental implementation of Fourier-transform spectral interferometry and its application to the study of spectrometers. *Applied Physics B*, **70**, S99.
- Dorrer, C., Belabas, N., Likforman, J.-P., and Joffre, M. (2000b) Spectral resolution and sampling issues in Fourier-transform

- spectral interferometry. *Journal of the Optical Society of America*, **17**, 1795.
- Eckle, P., Pfeiffer, A., Cirelli, C., Staudte, A., Dörner, R., Müller, H.G., Büttiker, M., and Keller, U. (2008a) Attosecond ionization and tunneling delay time measurements in helium. *Science*, **322**, 1525–1529.
- Eckle, P., Smolarski, M., Schlup, P., Biegert, J., Staudte, A., Schöffler, M., Müller, H.G., Dörner, R., and Keller, U. (2008b) Attosecond angular streaking. *Nature Physics*, **4**, 565–570.
- Eikema, K.S.E. and Ubachs, W. (2011) Precision laser spectroscopy in the extreme ultraviolet, in *Handbook of High-resolution Spectroscopy*, Quack, M. and Merkt, F. (eds), John Wiley & Sons, Ltd., Chichester, UK.
- Fermann, M.E., Galvanauskas, A., Sucha, G., and Harter, D. (1997) Fiber-lasers for ultrafast optics. *Applied Physics B*, **65**, 259–275.
- Ferray, M., L’huillier, A., Li, X.F., Lompré, L.A., Mainfray, G., and Manus, C. (1988) Multiple-harmonic conversion of 1064 nm radiation in rare gases. *Journal of Physics B*, **21**, L31–L35.
- Fittinghoff, D.N., Bowie, J.L., Sweetser, J.N., Jennings, R.T., Krumbügel, M.A., Delong, K.W., Trebino, R., and Walmsley, I.A. (1996) Measurement of the intensity and phase of ultraweak, ultrashort laser pulses. *Optics Letters*, **21**, 884–886.
- Fork, R.L., Martinez, O.E., and Gordon, J.P. (1984) Negative dispersion using pairs of prisms. *Optics Letters*, **9**, 150–152.
- Frey, H.-M., Kummlı, D., Lobsiger, S., and Leutwyler, S. (2011) High-resolution rotational Raman coherence spectroscopy with femtosecond pulses, in *Handbook of High-resolution Spectroscopy*, Quack, M. and Merkt, F. (eds), John Wiley & Sons, Ltd., Chichester, UK.
- Gaarde, M.B., Tate, J.L., and Schafer, K.J. (2008) Macroscopic aspects of attosecond pulse generation. *Journal of Physics B*, **41**, 132001.
- Gallmann, L., Pfeifer, T., Nagel, P.M., Abel, M.J., Neumark, D.M., and Leone, S.R. (2006) Comparison of the filamentation and the hollow-core fiber characteristics for pulse compression into the few-cycle regime. *Applied Physics B*, **86**, 561–566.
- Giesen, A., Hügel, H., Voss, A., Wittig, K., Brauch, U., and OPOWER, H. (1994) Scalable concept for diode-pumped high-power solid-state lasers. *Applied Physics B*, **58**, 365–372.
- Goulielmakis, E., Schultze, M., Hofstetter, M., Yakovlev, V.S., Gagnon, J., Uiberacker, M., Aquila, A.L., Gullikson, E.M., Attwood, D.T., Kienberger, R., *et al.* (2008) Single-cycle nonlinear optics. *Science*, **320**, 1614–1617.
- Hamm, P. (2011) 2D-infrared spectroscopy, in *Handbook of High-resolution Spectroscopy*, Quack, M. and Merkt, F. (eds), John Wiley & Sons, Ltd., Chichester, UK.
- Hänsch, T.W. (2006) Nobel lecture: passion for precision. *Reviews of Modern Physics*, **78**, 1297–1308.
- Hauri, C.P., Kornelis, W., Helbing, F.W., Heinrich, A., Couraıron, A., Mysyrowicz, A., Biegert, J., and Keller, U. (2004) Generation of intense, carrier-envelope phase-locked few-cycle laser pulses through filamentation. *Applied Physics B*, **79**, 673–677.
- Haus, H.A., Shank, C.V., and Ippen, E.P. (1975) Shape of passively mode-locked laser pulses. *Optics Communications*, **15**, 29.
- Holtom, G.R. (2006) Mode-locked Yb:KGW laser longitudinally pumped by polarization-coupled diode bars. *Optics Letters*, **31**, 2719–2721.
- Hönninger, C., Morier-Genoud, F., Moser, M., Keller, U., Brovelli, L.R., and Harder, C. (1998) Efficient and tunable diode-pumped femtosecond Yb:glass lasers. *Optics Letters*, **23**, 126–128.
- Hönninger, C., Paschotta, R., Graf, M., Morier-Genoud, F., Zhang, G., Moser, M., Biswal, S., Nees, J., Braun, A., Mourou, G.A., *et al.* (1999) Ultrafast ytterbium-doped bulk lasers and laser amplifiers. *Applied Physics B*, **69**, 3–17.
- Jones, R.J., Moll, K.D., Thorpe, M.J., and Ye, J. (2005) Phase-coherent frequency combs in the vacuum ultraviolet via high-harmonic generation inside a femtosecond enhancement cavity. *Physical Review Letters*, **94**, 193201.
- Kärtner, F.X., Jung, I.D., and Keller, U. (1996) Soliton mode-locking with saturable absorbers. *IEEE Journal of Selected Topics in Quantum Electron*, **2**, 540–556.
- Kärtner, F.X. and Keller, U. (1995) Stabilization of soliton-like pulses with a slow saturable absorber. *Optics Letters*, **20**, 16–18.
- Kärtner, F.X., Matuschek, N., Schibli, T., Keller, U., Haus, H.A., Heine, C., Morf, R., Scheuer, V., Tilsch, M., Tschudi, T., *et al.* (1997) Design and fabrication of double-chirped mirrors. *Optics Letters*, **22**, 831–833.
- Keller, U. (1999) Semiconductor nonlinearities for solid-state laser modelocking and Q-switching, in *Nonlinear Optics in Semiconductors*, Garmire, E. and Kost, A. (eds), Academic Press, Inc, Boston.
- Keller, U. (2003) Recent developments in compact ultrafast lasers. *Nature*, **424**, 831–838.
- Keller, U. (2007) Ultrafast solid-state lasers, in *Landolt-Börnstein. Laser Physics and Applications. Subvolume B: Laser Systems. Part I*, Herziger, G., Weber, H. and Proprawe, R. (eds), Springer-Verlag, Heidelberg.
- Keller, U., Knox, W.H., and Thooft, G.W. (1992) Ultrafast solid-state modelocked lasers using resonant nonlinearities. *IEEE Journal of Quantum Electronics*, **28**, 2123–2133.
- Keller, U., Thooft, G.W., Knox, W.H., and Cunningham, J.E. (1991) Femtosecond pulses from a continuously self-starting passively mode-locked Ti:Sapphire Laser. *Optics Letters*, **16**, 1022–1024.
- Keller, U., Weingarten, K.J., Kärtner, F.X., Kopf, D., Braun, B., Jung, I.D., Fluck, R., Hönninger, C., Matuschek, N., and Ausder Au, J. (1996) Semiconductor saturable absorber mirrors (SESAMs) for femtosecond to nanosecond pulse generation in solid-state lasers. *IEEE Journal of Selected Topics in Quantum Electronics*, **2**, 435–453.
- Klopp, P., Petrov, V., Griebner, U., and Erbert, G. (2002) Passively mode-locked Yb:KYW laser pumped by a tapered diode laser. *Optics Express*, **10**, 108–113.
- Kosik, E.M., Radunsky, A.S., Walmsley, I.A., and Dorrer, C. (2005) Interferometric technique for measuring broadband ultrashort pulses at the sampling limit. *Optics Letters*, **30**, 326–328.

- Lorenser, D., Unold, H.J., Maas, D.J.H.C., Aschwanden, A., Grange, R., Paschotta, R., Ebling, D., Gini, E., and Keller, U. (2004) Towards wafer-scale integration of high repetition rate passively mode-locked surface-emitting semiconductor lasers. *Applied Physics B*, **79**, 927–932.
- Mairesse, Y. and Quéré, F. (2005) Frequency-resolved optical gating for complete reconstruction of attosecond bursts. *Physical Review A*, **71**, 011401.
- Marchese, S.V., Baer, C.R.E., Engqvist, A.G., Hashimoto, S., Maas, D.J.H.C., Golling, M., Südmeyer, T., and Keller, U. (2008) Femtosecond thin disk laser oscillator with pulse energy beyond the 10-microjoule level. *Optics Express*, **16**, 6397–6407.
- Martinez, O.E. (1987) 3000 times grating compressor with positive group velocity dispersion: application to fiber compensation in 1.3–1.6 μm region. *IEEE Journal of Quantum Electronics*, **23**, 59–64.
- Martinez, O.E., Gordon, J.P., and Fork, R.L. (1984) Negative group-velocity dispersion using refraction. *Journal of the Optical Society of America*, **1**, 1003–1006.
- Merkt, F. and Quack, M. (2011) Molecular quantum mechanics and molecular spectra, molecular symmetry, and interaction of matter with radiation, in *Handbook of High-resolution Spectroscopy*, Quack, M. and Merkt, F. (eds), John Wiley & Sons, Ltd., Chichester, UK.
- Muller, H.G. (2002) Reconstruction of attosecond harmonic beating by interference of two-photon transitions. *Applied Physics B*, **74**, S17–S21.
- Nisoli, M., De Silvestri, S., Svelto, O., Szpöcs, R., Ferencz, K., Spielmann, C., Sartania, S., and Krausz, F. (1997) Compression of high energy laser pulses below 5 fs. *Optics Letters*, **22**, 522–524.
- Paschotta, R., Aus der Au, J., Spühler, G.J., Morier-Genoud, F., Hövel, R., Moser, M., Erhard, S., Karszewski, M., Giesen, A., and Keller, U. (2000) Diode-pumped passively mode-locked lasers with high average power. *Applied Physics B*, **70**, S25–S31.
- Paul, A., Gibson, E.A., Zhang, X., Lytle, A., Popmintchev, T., Zhou, X., Murnane, M.M., Christov, I.P., and Kapteyn, H.C. (2006) Phase-matching techniques for coherent soft X-Ray generation. *IEEE Journal of Quantum Electronics*, **42**, 14–26.
- Paul, P.M., Toma, E.S., Breger, P., Mullot, G., Augé, F., Balcou, P., Muller, H.G., and Agostini, P. (2001) Observation of a train of attosecond pulses from high harmonic generation. *Science*, **292**, 1689–1692.
- Paunescu, G., Hein, J., and Sauerbrey, R. (2004) 100-fs diode-pumped Yb:KGW mode-locked laser. *Applied Physics B*, **79**, 555–558.
- Perry, M.D. and Mourou, G. (1994) Terawatt to petawatt subpicosecond lasers. *Science*, **264**, 917–924.
- Pshenichnikov, M.S., Boeij, W.P.D., and Wiersma, D.A. (1994) Generation of 13-fs, 5-MW pulses from a cavity-dumped Ti:sapphire laser. *Optics Letters*, **19**, 572–574.
- Quack, M. (2011) Fundamental symmetries and symmetry violations from high-resolution spectroscopy, in *Handbook of High-resolution Spectroscopy*, Quack, M. and Merkt, F. (eds), John Wiley & Sons, Ltd., Chichester, UK.
- Rabitz, H., Vivie-Riedle, R.D., Motzkus, M., and Kompa, K. (2000) Whither the future of controlling quantum phenomena? *Science*, **288**, 824–828.
- Rausch, S., Binhammer, T., Harth, A., Kim, J., Ell, R., Kärtner, F.X., and Morgner, U. (2008) Controlled waveforms on the single-cycle scale from a femtosecond oscillator. *Optics Express*, **16**, 9739–9745.
- Saldin, E.L., Schneidmiller, E.A., and Yurkov, M.V. (2002) Scheme for attophysics experiments at a X-ray SASE FEL. *Optics Communications*, **212**, 377–390.
- Sansone, G., Benedetti, E., Calegari, F., Vozzi, C., Avaldi, L., Flammini, R., Poletto, L., Villoresi, P., Altucci, C., Velotta, R., et al. (2006) Isolated single-cycle attosecond pulses. *Science*, **314**, 443–446.
- Spence, D.E., Kean, P.N., and Sibbett, W. (1991) 60-fsec pulse generation from a self-mode-locked Ti:Sapphire laser. *Optics Letters*, **16**, 42–44.
- Steinmeyer, G., Sutter, D.H., Gallmann, L., Matuschek, N., and Keller, U. (1999) Frontiers in ultrashort pulse generation: pushing the limits in linear and nonlinear optics. *Science*, **286**, 1507–1512.
- Südmeyer, T., Marchese, S.V., Hashimoto, S., Baer, C.R.E., Ginzgras, G., Witzel, B., and Keller, U. (2008) Femtosecond laser oscillators for high-field science. *Nature Photonics*, **2**, 599–604.
- Sutter, D.H., Gallmann, L., Matuschek, N., Morier-Genoud, F., Scheuer, V., Angelow, G., Tschudi, T., Steinmeyer, G., and Keller, U. (2000) Sub-6-fs pulses from a SESAM-assisted Kerr-lens mode-locked Ti:sapphire laser: at the frontiers of ultrashort pulse generation. *Applied Physics B*, **70**, S5–S12.
- Szpöcs, R., Ferencz, K., Spielmann, C., and Krausz, F. (1994) Chirped multilayer coatings for broadband dispersion control in femtosecond lasers. *Optics Letters*, **19**, 201–203.
- Telle, H.R., Steinmeyer, G., Dunlop, A.E., Stenger, J., Sutter, D.H., and Keller, U. (1999) Carrier-envelope offset phase control: a novel concept for absolute optical frequency measurement and ultrashort pulse generation. *Applied Physics B*, **69**, 327–332.
- Teacy, E.B. (1969) Optical pulse compression with diffraction gratings. *IEEE Journal of Quantum Electronics*, **5**, 454–458.
- Trebino, R. (2002) *Frequency-resolved Optical Gating: The Measurement of Ultrashort Laser Pulses*, Kluwer Academic Publishers, Norwell.
- Tsakiris, G.D., Eidmann, K., Meyer-Ter-Vehn, J., and Krausz, F. (2006) Route to intense single attosecond pulses. *New Journal of Physics*, **8**, 1–20.
- Walmsley, I.A. (2004) Characterization of ultrashort optical pulses in the few-cycle regime using spectral phase interferometry for direct electric-field reconstruction, in *Few-Cycle Laser Pulse Generation and its Applications*, Kärtner, F.X. (ed). Springer, Berlin Heidelberg New York.
- Wörner, H.J. and Corkum, P.B. (2011) Attosecond spectroscopy, in *Handbook of High-resolution Spectroscopy*, Quack, M. and Merkt, F. (eds), John Wiley & Sons, Ltd., Chichester, UK.
- Zholents, A.A. and Fawley, W.M. (2004) Proposal for intense attosecond radiation from an X-Ray free-electron laser. *Physical Review Letters*, **92**, 224801.

RELATED ARTICLES

Eikema and Ubachs 2011: **Precision Laser Spectroscopy in the Extreme Ultraviolet**


Frey *et al.* 2011: **High-resolution Rotational Raman Coherence Spectroscopy with Femtosecond Pulses**

Hamm 2011: **2D-Infrared Spectroscopy**


Merkt and Quack 2011: **Molecular Quantum Mechanics and Molecular Spectra, Molecular Symmetry, and Interaction of Matter with Radiation**

Quack 2011: **Fundamental Symmetries and Symmetry Violations from High-resolution Spectroscopy**

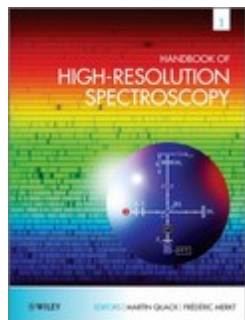
Wörner and Corkum 2011: **Attosecond Spectroscopy**

Browse our products:» **Books**Please specify 

Just published
Title search
Featured sites
Entertainment

Journals**Electronic Media****Choose your area of interest:**Please specify 

Merkt, Frederic

Handbook of High-resolution Spectroscopy

1. Edition - August 2011

710.- Euro**introductory price valid until 30. November 2011, thereafter**

870.- Euro

2011. 2182 Pages, 3 Volumes, Hardcover

- Handbook/Reference Book -

ISBN-10: 0-470-06653-9

ISBN-13: 978-0-470-06653-9 - John Wiley & Sons

**ORDER**[Online book](#)[Short description](#)[Detailed description](#)[Author affiliation](#)

0

Related books

[Handbook of Fluorescence Spectroscopy and Imaging](#)

From Single Molecules to Ensembles

[Applications of Vibrational Spectroscopy in Food Science](#)

[Reviews in Modern Astronomy Vol. 22](#)

Deciphering the Universe through Spectroscopy

[more >>]

Related journals

[European Journal of Lipid Science and Technology](#)

[Journal of Separation Science](#)

[Laser Physics Letters](#)

[more>>]

Special offer

Lüttge, Ulrich / Kluge, Manfred / Thiel, Gerhard

Short description

The field of High-Resolution Spectroscopy has been considerably extended and even redefined in some areas. Combining the knowledge of spectroscopy, laser technology, chemical computation, and experiments, Handbook of High Resolution Spectroscopies provides a comprehensive survey of the whole field as it presents itself today, with emphasis on the recent developments. This essential handbook for advanced research students, graduate students, and researchers takes a systematic approach through the range of wavelengths and includes the latest advances in these high-tech areas with great potential for future industrial development.





Botanik

69.- Euro

valid until

31 October 2011

[\[more offers >>\]](#)



[Tell a friend](#)



[RSS Feeds](#)

[Print-Version](#)

©2011 Wiley-VCH Verlag GmbH & Co. KGaA - [Provider](#)
<http://www.wiley-vch.de> - [mailto: info@wiley-vch.de](mailto:info@wiley-vch.de)
[Data Protection](#)